

# Seasonal overturning variability in the eastern North Atlantic subpolar gyre: A Lagrangian perspective

Oliver J. Tooth<sup>1</sup>, Helen L. Johnson<sup>1</sup>, Chris Wilson<sup>2</sup>, and Dafydd G. Evans<sup>3</sup>

<sup>1</sup>Department of Earth Sciences, University of Oxford, Oxford, United Kingdom

<sup>2</sup>National Oceanography Centre, Liverpool, United Kingdom

<sup>3</sup>National Oceanography Centre, Southampton, United Kingdom

**Correspondence:** Oliver J. Tooth (oliver.tooth@seh.ox.ac.uk)

**Abstract.** ~~Changes in the high-latitude~~ Both observations and ocean reanalyses show a pronounced seasonality in the strength of the Atlantic Meridional Overturning Circulation (MOC) ~~are dominated by water mass transformation in within~~ the eastern North Atlantic ~~Subpolar Gyre (SPG). Both observations and ocean reanalyses show a pronounced seasonality of the MOC within this region~~ subpolar gyre (eSPG). However, attributing this overturning seasonality to seasonal dense water formation ~~remains challenging owing to the wide distribution of recirculation timescales within the Iceland and Irminger basins.~~ Here, we investigate the nature of ~~this~~ seasonal overturning variability ~~within the eastern SPG~~ using Lagrangian water parcel trajectories ~~evaluated~~ initialised across the Overturning in the Subpolar North Atlantic Program (OSNAP) East section within an eddy-permitting ocean sea-ice hindcast ~~simulation.~~ Our analysis highlights the critical role of water parcel recirculation times in determining the seasonality of overturning measured in both the traditional Eulerian and complimentary Lagrangian frames of reference. ~~From an Eulerian.~~ By adopting a Lagrangian perspective, we show that the seasonal minimum of the ~~MOC seasonal eyele~~ Eulerian overturning at OSNAP East in autumn results from a combination of enhanced stratification and increased southward transport within the upper East Greenland Current. This convergence of southward transport within the MOC upper limb is explained by decreasing water parcel recirculation times in the upper Irminger Sea, consistent with a gyre-scale response to seasonal wind forcing. ~~From a Lagrangian perspective, we find that upper limb water parcels flowing northwards into the eastern SPG participate in a recirculation race against time to avoid wintertime diapycnal transformation into the lower limb of the MOC.~~ To account for the diversity of recirculation times within the eSPG, we also quantify the Lagrangian overturning (LMOC) as the total dense water formation along water parcel trajectories. The majority of water parcels, sourced from the central and southern branches of the North Atlantic Current, ~~are unsuccessful~~ fail to return to OSNAP East prior to experiencing wintertime diapycnal transformation into the lower limb, and thus determine the mean strength of ~~overturning within the eastern SPG~~ the LMOC within the eSPG ( $8.9 \pm 2.2$  Sv). The ~~seasonality of Lagrangian overturning~~ strong seasonality of the LMOC is explained by a small collection of upper limb water parcels, ~~recirculating~~ circulating rapidly ( $\leq 8.5$  months) in the upper Irminger and Central Iceland Basins, whose along-stream transformation is ~~dependent on their time of arrival in the eastern SPG~~ determined by their month of arrival at OSNAP East.

# 1 Introduction

25 The Atlantic Meridional Overturning Circulation (MOC) plays a critical role in the global climate system through the uptake and redistribution of heat, freshwater and anthropogenic carbon (McKinley et al., 2017; Bryden et al., 2020; Fay and McKinley, 2021; Li et al., 2021b). In the Subpolar North Atlantic (SPNA), the MOC is characterised by the transformation of warm, saline subtropical waters, transported northward in the North Atlantic Current (NAC), into cold, dense, carbon-rich waters flowing southward at depth (Buckley and Marshall, 2016). Traditionally, the formation of dense water masses feeding the lower limb of the MOC has been ascribed to open-ocean deep convection in the Labrador and Nordic Seas (e.g., Biastoch et al. 2008; Medhaug et al. 2012). However, a combination of both theoretical and observational studies have challenged this long-standing paradigm (Spall, 2004; Pickart et al., 2006), prompting a re-examination of the locations and mechanisms governing variations in the strength of subpolar overturning.

The At subpolar latitudes, the Overturning in the Subpolar North Atlantic Program (OSNAP) ~~was initiated in summer 2014 to complement the Rapid Climate Change — Meridional Overturning Circulation Heatflux Array (RAPID-MOCHA) along 26.5°N (Cunningham et al., 2007) by providing the first continuous measurements~~ has provided continuous estimates of the MOC at subpolar latitudes (Lozier et al., 2017). The OSNAP observing system ~~comprises two~~ since the summer of 2014 (Lozier et al., 2017; Li et al., 2017). By measuring the volume transport and hydrography along two trans-basin sections which extend across the Labrador Sea (OSNAP West) and the Irminger and Iceland Basins (OSNAP East) (Lozier et al., 2017; ?). The strength of the MOC is diagnosed directly from the volume transports and hydrography measured along the OSNAP array, thereby translating water mass transformation along the complex circulation pathways of the Subpolar Gyre (SPG) and the Nordic Seas overflows into a single quantity, zonally integrated at the basin scale (Lozier et al., 2019; Li et al., 2021a). In contrast with the subtropics (Frajka-Williams et al., 2019), the subpolar MOC is more appropriately calculated in density coordinates as the total transformation from lighter to denser water masses north of the OSNAP array (Lherminier et al., 2007; Holliday et al., 2007). This is because a substantial portion of subpolar overturning is due to the horizontal circulation of the SPG across sloping isopycnal surfaces (Zhang and Thomas, 2021; Hirschi et al., 2020), which cannot imprint onto the MOC calculated in depth coordinates.

~~The OSNAP data reveal~~ observing arrays, OSNAP has revealed that the mean strength and variability of the ~~MOC are~~ subpolar overturning circulation is dominated by dense water formation east of Greenland (north of OSNAP East; Fig. 1a), rather than in the Labrador Sea (Lozier et al., 2019; Li et al., 2021a). Further investigation of the sources of North Atlantic Deep Water (NADW) feeding the ~~MOC lower limb have~~ lower limb of the MOC has shown that dense water formation is distributed approximately equally between the Iceland and Irminger ~~Basins~~ basins and the Nordic Seas (Bringedal et al., 2018; Chafik and Rossby, 2019; Petit et al., 2020). ~~The deepest portion of the MOC lower limb, known as lower NADW, is sourced from dense overflow waters spilling over the Greenland-Scotland Ridge (Dickson and Brown, 1994; Eldevik et al., 2009). Overflow waters are formed by a combination of continuous surface buoyancy loss along the perimeter of the Nordic Seas (Mauritzen, 1996; Isachsen et al., 2008; Våge et al., 2011, 2015). Open-ocean convection also occurs in the southwestern Irminger Sea (Våge et al., 2008; Piron et al., 2016), resulting in the formation of a water mass with a similar composition to deep Labrador Sea Water (LSW) (Pickart et al., 1997; Rhein et al., 2015), known as deep Irminger Sea~~

Intermediate Water (ISIW) (Le Bras et al., 2020). Upper-ISIW, constituting the lightest component of the MOC lower limb (Le Bras et al., 2020), is instead formed by the progressive densification of Subpolar Mode Waters (SPMW) advected along the cyclonic pathways of the eastern SPG (Brambilla and Talley, 2008; Thierry et al., 2008). Crucially, it is variations in the production of upper and deep-ISIW however, it is variations in the production of upper NADW within the eastern Subpolar Gyre (eSPG; Fig. 1a), south of the Greenland-Scotland Ridge, which dominates the variability of the subpolar MOC subpolar overturning on monthly to decadal timescales (Petit et al., 2020; Desbruyères et al., 2019).

Throughout the North Atlantic Ocean, observational and modelling studies demonstrate that the variability of the MOC is larger on seasonal than interannual-decadal timescales (Willis, 2010; Mielke et al., 2013; Xu et al., 2014). At subpolar latitudes, observations reveal interannual timescales (Willis, 2010; Mielke et al., 2013; Xu et al., 2014; Lozier et al., 2019). In the eSPG, both observations and ocean reanalyses show a pronounced seasonality in the MOC (Mercier et al., 2015; Li et al., 2021a) (Mercier et al., 2015; Li et al., 2021a; Wang et al., 2021), which is closely related to the formation and export of seasonal western boundary density anomalies (Holte and Straneo, 2017; Le Bras et al., 2020). In particular, the recent modelling study of Wang et al. (2021) attributed the overturning seasonality at OSNAP East to the projection of seasonal density changes in the upper Irminger Sea onto the mean barotropic transport of the East Greenland Current (EGC). (Le Bras et al., 2020). Since the formation of dense waters exported southward in the EGC along the western boundary is principally governed by surface heat buoyancy loss over the Iceland and Irminger Basins basins (Brambilla and Talley, 2008; Petit et al., 2020; Pacini et al., 2020), we might anticipate a seasonal cycle of overturning at OSNAP East which closely reflects the seasonality of surface buoyancy forcing north of OSNAP East within this region. However, the observed amplitude of seasonal overturning variability ( $\sim 4$  Sv where  $1 \text{ Sv} \equiv 1 \times 10^6 \text{ m}^3 \text{ s}^{-1}$ ; Mercier et al. 2015; Li et al. 2021a) is typically 5 times smaller than the magnitude of seasonal surface-forced transformation within the eastern SPG buoyancy-driven transformation ( $\sim 20$  Sv; Xu et al. 2018a; Petit et al. 2020). While this difference is partially explained by large, compensating seasonal volume changes of the lightest water masses (Brambilla et al., 2008; Evans et al., 2017), overturning seasonality also remains small compared with the observed mean strength of the MOC ( $\sim 16$  Sv) in the eastern SPNA (Sarafanov et al., 2012; Mercier et al., 2015; Lozier et al., 2019; Xu et al. 2018b; Petit et al. 2020). This difference reflects the fact that overturning variability depends upon both the transformation of water masses into the lower limb of the MOC and the rate at which they are subsequently exported southward across the OSNAP East section. Given that water masses circulate on timescales ranging from weeks to years within the eSPG (Tooth et al., 2023), it therefore remains an open question to what extent the overturning seasonality measured at OSNAP East can be attributed to seasonal dense water formation.

In addition to The recent modelling study of Wang et al. (2021) attributes the seasonality of overturning at OSNAP East to the projection of seasonal density changes in the western Irminger Sea onto the time-mean barotropic transport of the East Greenland Current (EGC). On the one hand, this is consistent with OSNAP observations, which reveal strong seasonality in the thickness of upper Irminger Sea Intermediate Water (ISIW; the lightest component of the MOC lower limb) exported southward in the EGC during 2014-18 (Le Bras et al., 2020; Li et al., 2021a). However, on the other hand, observations also show pronounced seasonality in the volume transport of the western boundary current, which is closely correlated with the seasonality of wind stress curl over the Irminger Sea (Daniault et al., 2011a, b; Le Bras et al., 2018; Pacini et al., 2020). To our

knowledge, no study to date has explored how such seasonal changes in both the density structure and transport of the EGC might act in combination to modulate the seasonality of overturning measured at OSNAP East.

95 In the traditional Eulerian overturning framework discussed above, ~~seasonal variations in the formation of dense water north of OSNAP East, the recent study of Le Bras et al. (2020) demonstrates that seasonal overturning variability is closely related to the timescales of subduction and export within the western boundary current of the Irminger Sea. In particular, the authors showed that~~ predicated upon the efficient export of lower limb water masses within several months of their formation upstream. At OSNAP East, Le Bras et al. (2020) showed that overturning seasonality is preferentially determined by variations  
100 in the formation rate of upper ISIW ~~formed in the vicinity of the boundary current can contribute significantly to overturning seasonality since upper ISIW is rapidly exported across OSNAP East in several months. Meanwhile~~ due to its rapid export southward within the EGC (Pacini et al., 2020). In contrast, variability in the formation rate of deep ISIW formed in the Irminger Sea interior ~~projects onto interannual~~ was found to imprint onto interannual Eulerian overturning variability owing to its slower entrainment into the ~~western boundary current (Le Bras et al., 2020). The dominant role of upper ISIW in driving~~  
105 ~~seasonal overturning variability at OSNAP East has since been further highlighted by Li et al. (2021a), who revealed strong seasonality in the observed thickness of upper ISIW in both the EGC and the Irminger Sea interior between 2014-2018. While the aforementioned studies have successfully identified the final water mass properties associated with seasonal overturning variability in the eastern SPNA, we have yet to establish the origins of seasonally transformed water masses along the OSNAP East section. It therefore remains an open question whether there is a clear distinction between the pathways and advective~~  
110 ~~timescales of water masses contributing substantially to~~ boundary current (Le Bras et al., 2020; Li et al., 2021a). Given the diversity of export times convolved in the mean strength of the MOC compared with those responsible for its variability on ~~seasonal timescales.~~

~~In this study, we investigate the nature of seasonal overturning variability in the eastern SPG using a Lagrangian particle tracking tool in conjunction with an eddy-permitting, global ocean sea-ice hindcast simulation. Extending the Lagrangian overturning framework recently introduced by ?, we use water parcel trajectories, initialised in the northward inflows across a model-defined OSNAP East array, to determine the distribution of seasonal overturning variability across the cyclonic circulation pathways of the eastern SPG. Moreover, we demonstrate the critical role of water parcel recirculation times within the eastern SPG in shaping the seasonal cycles of both the Lagrangian and Eulerian overturning evaluated~~ western boundary current of the Irminger Sea, it is perhaps therefore unsurprising that changes in the velocity and density field of the EGC alone  
120 have been shown to account for only 10% of the monthly MOC variability at OSNAP East (Li et al., 2021a).

One way to better understand the relationship between seasonal buoyancy-driven transformation and the overturning seasonality recorded at OSNAP East is to explicitly account for the diverse range of water mass export timescales by adopting a Lagrangian frame of reference. In the recent study of Tooth et al. (2023), the authors introduced a novel Lagrangian measure of the density-space overturning by quantifying the total dense water formation along water parcel trajectories flowing northward  
125 across the OSNAP East section. Here, we extend this Lagrangian overturning framework to identify the circulation pathways responsible for seasonal overturning variability at OSNAP East and characterise their advective timescales and along-stream transformations within the eSPG.



The manuscript is structured as follows. We begin by introducing the numerical model simulation, Lagrangian particle tracking approach, and defining ~~the both the Eulerian and Lagrangian~~ overturning in density-space at OSNAP East in Section 2. ~~The simulated seasonal variability of the MOC~~ Section 3 explores the seasonal Eulerian overturning variability simulated at OSNAP East ~~is explored from both Eulerian and Lagrangian perspectives in Section 3. Section~~ and addresses the physical mechanisms responsible, including the important role of seasonal water parcel recirculation times in the upper Irminger Sea. In Section 4 ~~diagnoses the origins and~~, we introduce a complementary Lagrangian measure of overturning variability at OSNAP East and ~~diagnose the~~ advective timescales of water parcels contributing to the mean strength and seasonality of Lagrangian overturning. In Section 5, we ~~We also~~ decompose the seasonal cycle of Lagrangian overturning by circulation pathway, and examine the role of along-stream diathermal and diahaline transformations in driving seasonal ~~water mass modification. Section 6 addresses the mechanisms of seasonal Eulerian overturning variability, including the important role of water parcel recirculation times in the upper Irminger Sea. dense water formation.~~ The manuscript concludes with a discussion of our principal findings in Section 7-5.

## 2 Model and methods

### 2.1 Model description

In this study we use output from the ORCA025-GJM189 ocean-sea-ice hindcast simulation produced by the Drakkar initiative (Barnier et al., 2006). The simulation uses a global implementation of the Nucleus for European Modeling of the Ocean (NEMO) model coupled to the thermodynamic Louvain-la-Neuve Ice Model version 2 (LIM2) (Fichefet and Morales Maqueda, 1999). The ocean is simulated using the eddy-permitting ORCA025 configuration of the NEMO v3.5 model (Madec, 2014), which utilises the ORCA tripolar grid configured with a nominal horizontal resolution of  $1/4^\circ$  (27.75 km at the equator,  $\sim 12$  km in the Arctic) and 75 unevenly spaced z-coordinate levels in the vertical. Sub-grid scale parameterisations include horizontal biharmonic viscosity for momentum, Laplacian isopycnal diffusivity for tracers, and the TKE turbulent closure scheme for vertical mixing (Barnier et al., 2006). A comprehensive description of the ORCA025-GJM189 configuration can be found in Molines (2021).

The ORCA025-GJM189 hindcast used here simulates the historical period from 1958-2015, initialised from rest. Atmospheric forcing is computed using the CORE bulk formulae and the Drakkar Forcing Set 5.2, which combines surface fluxes from the ERA40 (Uppala et al., 2005) and ERA-Interim reanalyses (Dee et al., 2011). The initial conditions of the simulation are provided by a combination of the Levitus climatological hydrography (Levitus et al., 1998) and the Polar Science Center Hydrographic Climatology (Steele et al., 2001) in the Arctic. A relaxation of sea surface salinity to the Levitus climatological hydrography with a piston velocity of  $167 \text{ mm day}^{-1}$ , equivalent to a 60 day decay time for 10 m of water depth (Molines, 2021), is included to minimise model drift. Following the approach of MacGilchrist et al. (2020), the first 18 years are discarded, to allow for spin-up. The period 1976-2015 is analysed using 5-day ~~model-mean-mean model~~ output.

There are several motivations for choosing to use the ORCA025-GJM189 hindcast simulation in this study. Firstly, this specific ocean sea-ice hindcast has been used in multiple previous Lagrangian analyses investigating the circulation of the

subpolar North Atlantic ocean (Asbjørnsen et al., 2021; MacGilchrist et al., 2020, 2021; Tooth et al., 2023). Secondly, the ORCA025-GJM model is configured at a nominal horizontal resolution ( $1/4^\circ$ ), which is approximately four times finer than the typical resolution used in the ocean component of CMIP6 climate models (e.g. Heuzé 2021) and is more typical of the climate models involved in the upcoming CMIP7 analysis. Thus, understanding how such eddy-permitting models represent seasonal to interannual subpolar overturning variability is crucial if we are to have confidence in their ability to project future trends in the MOC. Finally, the ORCA025 model configuration has been validated extensively within the subpolar North Atlantic by previous studies exploring the strength and variability of the gyre and overturning circulations on seasonal to multidecadal timescales (e.g. Asbjørnsen et al. 2021; Desbruyères et al. 2013, 2015; de Boissésion et al. 2010, 2012; MacGilchrist et al. 2020; Tooth et al. 2023).

In the eSPG specifically, Tooth et al. (2023) found good agreement between the summertime upper ocean transports across the OSNAP East section in the ORCA025-GJM189 simulation and the observations of Sarafanov et al. (2010) at  $59.5^\circ\text{N}$ . Moreover, both Tooth et al. (2023) and de Boissésion et al. (2012) have highlighted the close agreement between the simulated water mass properties of Subpolar Mode Waters (SPMW) transformed at the surface of the eSPG at eddy-permitting resolution and those observed by Brambilla and Talley (2008) and Thierry et al. (2008). Model biases primarily emerge at depth in the ORCA025-GJM189 simulation, where there is an absence of deep stratification within the eSPG due to excessive mixing between the Nordic seas overflows and ambient Atlantic water masses south of the Greenland-Scotland Ridge (MacGilchrist et al., 2020; Tooth et al., 2023). In spite of this, the ORCA025 configuration was chosen by Li et al. (2017) to assess the extent to which observed measurements can faithfully represent fluxes across the OSNAP section, underscoring its ability to reproduce the primary features of the subpolar circulation.

## 2.2 Lagrangian particle tracking

To evaluate the trajectories of numerical water parcels advected by the time-varying velocity fields of the ORCA025-GJM189 hindcast, we use the Lagrangian offline particle tracking tool TRACMASS (v7.1, Aldama-Campino et al. 2020). TRACMASS determines the trajectory of each water parcel using a stepwise-stationary scheme, which divides the time between successive 5-day mean velocity fields into a series of intermediate time steps. The velocity field at each intermediate time step is determined by linear interpolation and is assumed to be steady for the duration of the step (Döös et al., 2017). A water parcel's trajectory path through each model grid cell can therefore be determined analytically whilst conserving the mass contained within each grid cell (Döös et al., 2013). As such, and because the ocean model is Boussinesq, the volume transport conveyed by each particle is conserved along its entire trajectory. For a comprehensive description of TRACMASS and its associated trajectory schemes readers are referred to Döös et al. (2017).

We make use of the Lagrangian experiment documented in ?Tooth et al. (2023), in which numerical water parcels are initialised in the northward inflows across the OSNAP East section (defined as in Menary et al. 2020) at-on the earliest available day of each month (based on the centre of the nearest 5-day mean window) for a period of 33 years (1976-2008). In total, more than 11.2 million water parcels are initialised, sampling the entire northward transport across OSNAP East over-for 396 months. During each monthly initialisation, the strategy for particle release is to distribute particles in proportion to the volume

195 transport through each grid cell, with a minimum of one particle per cell. An increment of 2.5 mSv per particle, per cell is used. Once initialised, water parcels are advected solely by the time-evolving velocity field except when found inside the surface mixed layer. Here, we parameterise the effects of vertical convective mixing by introducing random vertical displacements along water parcel trajectories (Paris et al., 2013), governed by a maximum vertical velocity of  $|w| = 10 \text{ cm s}^{-1}$  following Georgiou et al. (2021). Water parcels are removed from the experiment on meeting any one of three conditions: (i) on returning  
 200 to the OSNAP East section (red trajectories in Fig. 1a), (ii) on crossing the Greenland-Scotland Ridge northwards (green tra-  
 jectories in Fig. 1a), or (iii) upon reaching the maximum advection time of 7 years. Our decision to terminate water parcels on reaching the Greenland-Scotland Ridge is motivated by recent observations which show that monthly overturning variability at OSNAP East is dominated by surface buoyancy forcing over the Iceland and Irminger Basins rather than by variations in the overflow transport exiting the Nordic Seas (Bringedal et al., 2018; Østerhus et al., 2019; Petit et al., 2020). It should also be  
 205 noted that  $> 99.1\%$  of water parcels are intercepted on crossing either OSNAP East or the Greenland-Scotland Ridge within the 7-year maximum advection time. The remaining 0.9% of water parcels almost exclusively circulate at depth within the lower limb of the MOC north of OSNAP East and therefore do not contribute to the strength of overturning.

The position, potential temperature and salinity of each water parcel is output at every grid cell crossing north of OSNAP East and south of the Greenland-Scotland Ridge. Given that tracer variables are defined at the center of each grid cell, TRACMASS uses a linear interpolation scheme in time and space to determine water parcel properties from the two nearest model T points. The potential density referenced to the surface is then computed using the EOS-80 nonlinear equation of state (Fofonoff and Millard, 1983) consistent with our ORCA025 configuration of NEMO (Madec, 2014).

### 2.3 Definitions of the overturning in density-space

We use two complementary measures of the overturning in potential density-space at OSNAP East in this study. The Eulerian  
 215 overturning streamfunction,  $\psi(\sigma, t)$ , is calculated directly from the time-evolving velocity and potential density fields along the OSNAP East section following Lozier et al. (2019):

$$\psi(\sigma, t) = \int_{\sigma_{min}}^{\sigma} \int_{x_w}^{x_e} v(x, \sigma, t) dx d\sigma \quad (1)$$

where  $v(x, \sigma, t)$ , the velocity normal to the model-defined OSNAP East section (positive values represent northward trans-  
 220 ports), is first integrated from the east coast of Greenland ( $x_w$ ) to the Scottish shelf ( $x_e$ ). We then obtain the Eulerian overturning streamfunction with respect to potential density,  $\psi(\sigma, t)$ , by integrating from the sea surface ( $\sigma_{min}$ ) to a particular isopycnal layer ( $\sigma$ ).

We denote the isopycnal at which the Eulerian overturning streamfunction reaches a maximum as  $\sigma_{MOC}$ , representing the interface between the upper and lower limbs of the MOC at OSNAP East. The maximum overturning, measuring the overall strength of the MOC, therefore equates to the net northward transport within the upper limb integrated along the section. To

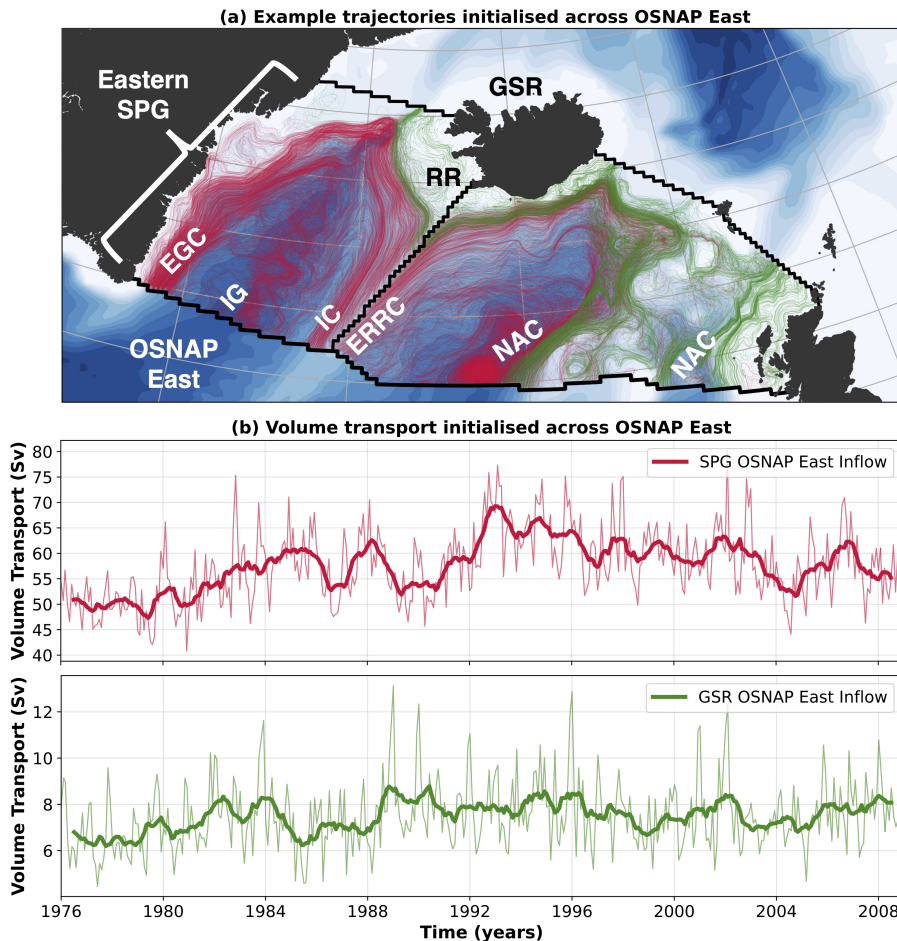


**Figure 1.** Lagrangian trajectories and volume transports across [the model-defined OSNAP East section](#). (a) Example Lagrangian trajectories initialised on the northward inflows across OSNAP East in January 1990. Trajectories of water parcels which recirculate back to OSNAP East within the [eastern-SPG-eSPG](#) (south of the Greenland-Scotland Ridge) are shown in red, whereas green trajectories represent water parcels which cross the Greenland-Scotland Ridge northwards as Atlantic inflows to the Nordic Seas. (b) Monthly volume transports initialised on the northward inflows across OSNAP East which recirculate within the [eastern-SPG-eSPG](#) (red, upper panel) and those which cross the Greenland-Scotland Ridge northwards (green, lower panel). The bold lines overlaid are low pass filtered volume transports using a 1-year running mean. ~~The grey dashed line indicates the volume transports across OSNAP East in January 1990.~~

225 ensure comparability between our analyses, Eulerian overturning streamfunctions are computed on the earliest available day of each month between 1976-2008.

[An important consideration when calculating the Eulerian overturning streamfunction at OSNAP East is how to account for the variability of net throughflow to the Arctic, which is not transformed into the lower limb of the MOC. In Lozier et al. \(2019\), a prescribed net throughflow of  \$+1.6 \pm 0.2\$  Sv is applied across the OSNAP East section to ensure a zero net meridional mass](#)

230 [transport across the combined OSNAP East and West sections. Here, as in Menary et al. \(2020\), we choose not to compensate for the variations in the net throughflow across OSNAP East since this would prevent us from investigating the transport structure of the MOC upper limb in Section 3.2. Critically, we find no seasonal signal in the net throughflow across the OSNAP East section and hence its inclusion in the Eulerian overturning streamfunction does not impact the findings of our study.](#)

To complement the Eulerian density-space overturning, we additionally diagnose the strength of the overturning at OSNAP East using a Lagrangian measure recently introduced by [Tooth et al. \(2023\)](#). The Lagrangian Overturning Function (LOF),  $F(\sigma, t, \tau_{max})$ , quantifies the total light-to-dense transformation occurring along water parcel trajectories flowing northward across OSNAP East at the earliest available day of each month. To compute  $F(\sigma, t, \tau_{max})$ , we first extract the 9.8 million water parcels which recirculate back to OSNAP East within the [eastern-SPG-eSPG](#) (south of the Greenland-Scotland Ridge) to form 396 trajectory ensembles, one for each month between 1976-2008 [\(Fig. 1b\)](#). For each monthly ensemble containing  $N$  water parcels, the LOF is given by [an equation describing the mass overturning across each isopycnal,  \$\sigma\$ , by water parcels having been initialised on the northward inflow of OSNAP East at time  \$t\$  and advected for a time  \$\tau\$  before flowing southward across the section:](#)

$$F(\sigma, t, \tau_{max}) = \int_{\sigma_{min}}^{\sigma} V_{North}(\sigma, t) - V_{South}(\sigma, t + \tau_{max}) d\sigma \quad (2)$$

where  $V_{North}$  represents the volume transport distribution of the ensemble water parcels in density-space on their northward crossing of the OSNAP East section at time  $t$ . This is calculated by integrating the absolute volume transports ( $V_n$ ) of the  $N$  water parcels in discrete potential density bins, where the bin width  $\Delta\sigma$  is prescribed as  $0.01 \text{ kg m}^{-3}$ . Once the ensemble of water parcels have been advected for a maximum of  $\tau_{max} \tau = \tau_{max} = 7$  years, we construct an equivalent volume transport distribution in density-space,  $V_{South}$ , using the properties of water parcels on their southward crossing of the OSNAP East section at time  $t + \tau$ , where  $0 < \tau \leq \tau_{max}$ . Since the volume transport conveyed by each water parcel is conserved along its trajectory, the total northward and southward transports across OSNAP East due to recirculating water parcels are equal in the Lagrangian overturning calculation, and thus there is no net flow across the section. The LOF for each monthly ensemble is obtained by taking the cumulative sum of the net volume transport distribution (i.e.,  $V_{North}(\sigma, t) - V_{South}(\sigma, t + \tau_{max})$   $V_{South}(\sigma, t + \tau)$ ) from the surface to the ocean floor. In keeping with its Eulerian counterpart, the strength of Lagrangian overturning (LMOC) is given by the maximum of the LOF, which occurs at the isopycnal of maximum Lagrangian overturning  $\sigma_{LMOC}$ . [We note that the strength and variability of the LMOC is not sensitive to our chosen parameterisation of vertical convective mixing along water parcel trajectories in the surface mixed layer, and therefore its inclusion does not impact the conclusions of this study.](#)

### 3 Seasonal overturning variability ~~at OSNAP East: An Eulerian perspective~~

#### 3.1 ~~Seasonal Eulerian overturning at OSNAP East~~

We begin by exploring the ~~seasonal variations in time-mean strength of~~ the density-space overturning at OSNAP East in  
260 ORCA025-GJM189 from ~~both Eulerian and Lagrangian perspectives.~~

#### 3.2 ~~The Eulerian perspective~~

~~the traditional Eulerian perspective.~~ Over the duration of the study period (1976-2008), the time-mean strength of the monthly  
MOC at OSNAP East is  $16.6 \pm 2.7$  Sv in ORCA025-GJM189, corresponding closely with observed estimates of the MOC  
at both  $59.5^\circ\text{N}$  ( $16.6 \pm 1.1$  Sv in 2002-2008; Sarafanov et al. 2012) and OSNAP East ( $16.8 \pm 0.6$  Sv in 2014-2018; Li  
265 et al. 2021a). The mean isopycnal of maximum Eulerian overturning ( $\sigma_{MOC} = 27.52 \text{ kg m}^{-3}$ ) is lighter in the simulation  
compared with observations ( $27.55 \text{ kg m}^{-3}$ ), owing to the shoaling of the SPNA overturning cell in response to the excessive  
entrainment of ambient Atlantic water by the Nordic seas overflows in the model (MacGilchrist et al., 2020). As shown  
in ~~?~~[Tooth et al. \(2023\)](#), the simulated mean net throughflow to the Arctic Ocean at OSNAP East is  $1.2 \pm 1.1$  Sv, in close  
agreement with the 1.0-1.6 Sv required by inverse models (~~?~~[Lherminier et al., 2007](#))([Li et al., 2017](#); [Lherminier et al., 2007](#)).

270 On subtracting this net throughflow from the mean strength of the MOC, we find that, on average, 15.4 Sv of upper limb waters  
are overturned north of OSNAP East in this simulation.

Figure 2a shows that the strength of the MOC at OSNAP East exhibits variability on monthly to interannual timescales.  
Concordant with the previous studies of Lozier et al. (2019) and Mercier et al. (2015), we find that MOC variability ~~in the~~  
~~eastern SPNA at OSNAP East~~ is most pronounced on monthly timescales ( $\text{SD} = \pm 2.7$  Sv), where monthly MOC values  
275 range from 7.8 Sv in October 1978 to 28.7 Sv in January 1996. The simulated MOC variability ~~at OSNAP East~~ is weaker on  
interannual timescales ( $\text{SD}$  of annual means =  $\pm 1.0$  Sv), in agreement with previous results from ocean models and reanalyses  
(Xu et al., 2014; Wang et al., 2021). The gradual increase in the MOC from the 1970s to the mid-1990s ( $+0.1 \text{ Sv yr}^{-1}$ ,  $p < 0.01$ )  
and the subsequent marked decline in the MOC between 1996 and 2000 ( $-1.3 \text{ Sv yr}^{-1}$ ,  $p < 0.01$ ) are well-documented trends,  
consistently found in both observations (Kieke et al., 2007; Mercier et al., 2015) and numerical modelling studies (Böning  
280 et al., 2006; Desbruyères et al., 2013; Xu et al., 2013).

The intra-annual variability in the MOC at OSNAP East is dominated by the strong seasonal cycle shown in Figure 2b. The  
peak-to-peak amplitude of the seasonal cycle is 4.1 Sv, in close ~~correspondence agreement~~ with the 4.2 Sv found by Wang  
et al. (2021) using a  $1/12^\circ$  Global Ocean Physics Reanalysis (1993-2016) and the 4.3 Sv seasonal cycle recorded along the  
OVIDE section (1993-2010) by Mercier et al. (2015). Figure 2b indicates that, on average, the MOC reaches a maximum  
285 in April (18.5 Sv) and a minimum in October (14.4 Sv). We note that, while there is strong consensus that the subpolar  
MOC reaches a maximum in spring (e.g. Holte and Straneo 2017; Li et al. 2021a), the occurrence of the seasonal MOC  
minimum during autumn in this simulation disagrees with the findings of previous reanalysis (August; Wang et al. 2021) and  
observational (December; Mercier et al. 2015) studies. One possible reason for this inconsistency between studies is that the  
MOC seasonal cycle, when computed from monthly composites, is non-stationary, such that the timing of the seasonal extrema



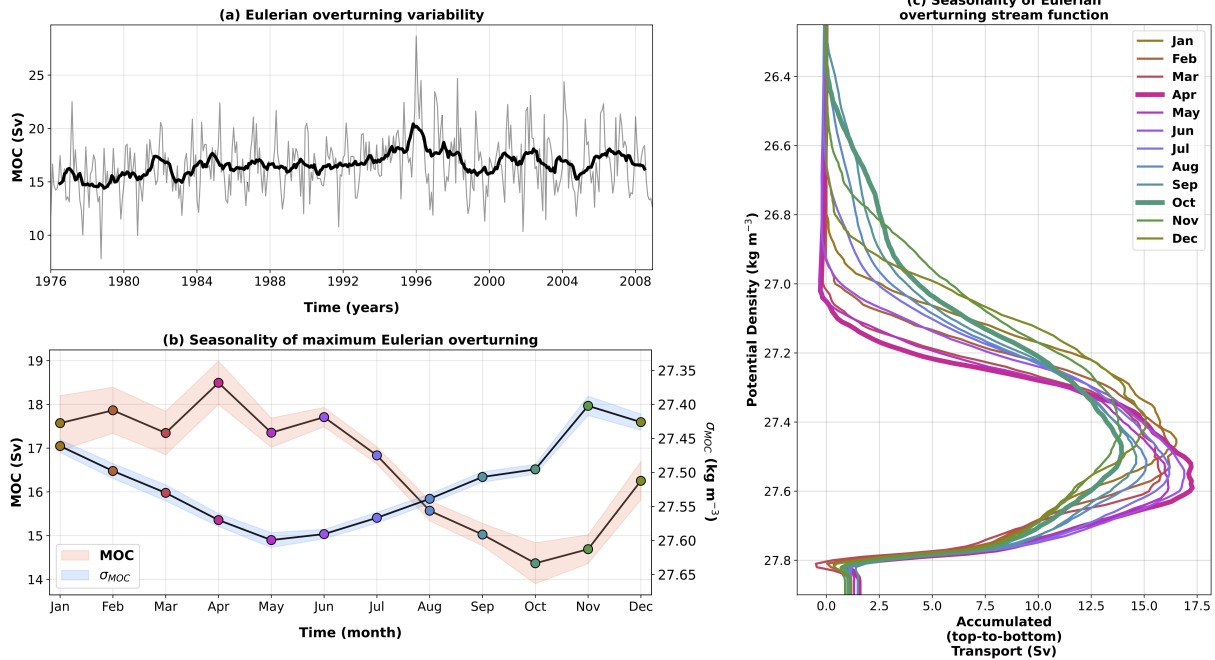


**Figure 2.** Eulerian overturning variability at the model-defined OSNAP East section. (a) Monthly maximum of the Eulerian overturning streamfunction in density-space (first available day of each month, grey line) and 1 year annual running mean (black bold line) overlaid for 1976-2008. (b) Mean seasonal cycles of the maximum of the Eulerian overturning streamfunction and the isopycnal of maximum overturning ( $\sigma_{MOC}$ ) computed from monthly composites. Shading represents  $\pm 1$  standard error of the monthly estimates. (c) Monthly composites of the Eulerian overturning streamfunction calculated in discrete density-space (bin width is  $0.01 \text{ kg m}^{-3}$ ); maximum (April) and minimum (October) months in the MOC seasonal cycle are included in bold.

290 will be dependent upon the years chosen to compute those composites. This is particularly notable in the results of Wang et al. (2021), where the most probable timing of the minimum of the MOC seasonal cycle at OSNAP East transitions from autumn during the years overlapping our study period (1993-2008) to summer between 2009-2016.

Given that the strength of the MOC equates to the net transport above  $\sigma_{MOC}$ , seasonal variations in the MOC can be attributed to either changes in the meridional velocity field or to changes in the **isopeynal-isopycnal** structure at OSNAP East. **Figure 2b shows that  $\sigma_{MOC}$  exhibits a pronounced seasonal cycle (peak-to-peak amplitude is  $0.2 \text{ kg m}^{-3}$ ) at OSNAP East, which lags seasonality in the strength of the MOC by 1 month. Although often overlooked, seasonal variations in  $\sigma_{MOC}$  provide valuable insight into** **To understand** how the composition of the MOC upper limb evolves on **intra-annual timescales. To explore this further** **seasonal timescales**, Figure 2c presents monthly composites of the Eulerian overturning streamfunction evaluated at OSNAP East. **It should be noted** **We note** that the maximum values of the monthly mean streamfunctions presented in Figure 2c underestimate the mean strength of the MOC determined from the maxima of monthly mean streamfunctions in **300** Figure 2b (Lozier et al., 2019). This is because the isopycnal of maximum overturning,  $\sigma_{MOC}$ , can vary substantially within

each of the monthly composites (Lozier et al., 2019). Figure 2c shows that the seasonal maximum of the MOC seasonal-eye in April occurs when upper limb waters flowing northwards across OSNAP East are relatively cold and dense ( $\sigma_{MOC} = 27.57$  in Fig. 2b) having experienced intense surface buoyancy loss along the NAC during the previous winter (Grist et al., 2016).  
 305 Conversely, the minimum of the MOC seasonal cycle in October is characterised by the arrival of warm and light upper limb waters ( $\sigma_{MOC} = 27.50$  in Fig. 2b) which have been transformed by summertime buoyancy gain in the NAC during the months prior (Li et al., 2021b).

The seasonal cycle in the strength of the MOC of Eulerian overturning at OSNAP East therefore corresponds to the expansion (MOC weakening in summer-autumn) and contraction (MOC strengthening in winter-spring) of the overturning streamfunction  
 310 in density-space, which is consistent with seasonal variations in surface buoyancy forcing over the NAC upstream.

### 3.2 The Lagrangian perspective Mechanisms of seasonal Eulerian overturning variability

~~The Lagrangian overturning~~ To identify the mechanisms responsible for seasonal Eulerian overturning variability, we next decompose the net transport of the MOC upper limb, determined directly from the simulated velocity and potential density fields along OSNAP East, into its constituent northward and southward components during April and October (corresponding  
 315 to the extrema of the MOC seasonal cycle in Figure 2b). Figure 3 indicates that, in spite of the year-round net northward transport in the upper limb, the seasonal cycle of the MOC results from changes in the southward transport above  $\sigma_{MOC}$  at OSNAP East. This is highlighted in Figure 3c, which shows that the total southward transport in the upper limb increases significantly from -8.7 Sv in April, when the Eulerian overturning reaches its seasonal maximum, to -14.4 Sv when the MOC seasonal minimum occurs in October.

**Table 1.** Mean Eulerian net volume transport (Sv) in the upper limb of the MOC (i.e., above  $\sigma_{MOC}$ ) for the major currents along the OSNAP East array during April and October. The major currents are defined geographically as follows: East Greenland Current (EGC,  $0 \text{ km} < x < 250 \text{ km}$ ), Irminger Gyre and Irminger Current (IG & IC,  $250 \text{ km} < x < 750 \text{ km}$ ), East Reykjanes Ridge Current (ERRC,  $750 \text{ km} < x < 1000 \text{ km}$ ), Central Iceland Basin and Sub-Arctic Front (CIB & SAF,  $1000 \text{ km} < x < 1450 \text{ km}$ ), and Rockall Plateau and Rockall Trough (RP & RT,  $1450 \text{ km} < x < 2300 \text{ km}$ ). Note  $x$  corresponds to the distance from Cape Farewell on the east Greenland coast.

	EGC	IG & IC	ERRC	CIB & SAF	RT & RP	Total
<b>Net Upper Limb</b>						
<b>Volume Transport (Sv)</b>						
April	-2.1	2.4	-2.5	14.2	6.5	18.5
October	-4.9	4.2	-4.2	13.9	5.4	14.4

320 By further decomposing the seasonal upper limb transport according to the major currents crossing the OSNAP East array (Table 1), we find that the seasonal minimum of the MOC results from the combination of a 2.8 Sv strengthening of the EGC southward transport above  $\sigma_{MOC}$  and a 1.1 Sv weakening of the southern NAC branch feeding the Rockall Trough and Plateau. This agrees with the recent results of Wang et al. (2021), who demonstrated that variations in the southward transport along

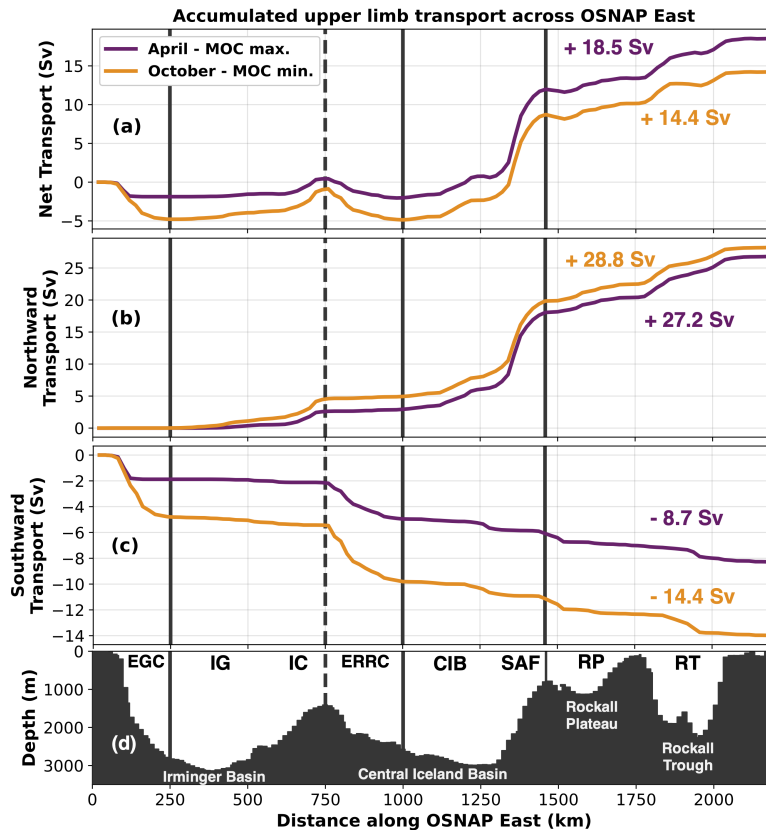


**Figure 3.** Mean Eulerian overturning variability at volume transport in the upper limb (i.e. above  $\sigma_{MOC}$ ) of the MOC accumulated with distance eastward along the model-defined OSNAP East section. The net upper limb volume transport (a) Monthly maximum of the Eulerian overturning streamfunction in density space is decomposed into its respective northward (first available day of each month, grey line) and 1-year annual running mean southward components (black bold line) overlaid for 1976–2008. The model bathymetry along the OSNAP East array is presented in (d) Mean seasonal cycles of. Vertical lines partition the maximum of volume transport across the Eulerian overturning streamfunction and section into five geographical regions corresponding to the isopycnal of maximum overturning ( $\sigma_{MOC}$ ) computed from monthly composites. Shading represents  $\pm 1$  standard error of major currents intercepted by the monthly estimates. array: East Greenland Current (eEGC) Monthly composites of the Eulerian overturning streamfunction calculated in discrete density space, Irminger Gyre and Irminger Current (bin width is  $0.01 \text{ kg m}^{-3}$  IG & IC); maximum, East Reykjanes Ridge Current (April ERRC), the Central Iceland Basin and minimum Sub-Arctic Front (October CIB & SAF) months in-, and the MOC seasonal cycle are included in bold Rockall Plateau and Rockall Trough (RP & RT).

325 the western boundary of the Irminger Sea play a prominent role in modulating the seasonal cycle of overturning at OSNAP East. Moreover, Wang et al. (2021) showed that the seasonality of the EGC upper limb transport is principally explained by seasonal density changes in the upper Irminger Sea projecting onto the mean barotropic transport of the western boundary current. To explore this further, Figure 4 presents the mean potential density field along OSNAP East in April and October and

the corresponding locations of  $\sigma_{MOC}$ . In April, we find that the erosion of stratification, owing to intense wintertime heat loss, permits deep convective mixing in the Irminger Sea interior (de Jong et al., 2012; de Jong and de Steur, 2016; Piron et al., 2016), such that  $\sigma_{MOC}$  ( $27.57 \text{ kg m}^{-3}$  in April) outcrops at the surface (Fig. 4a). As a consequence, there is a reduction in the total upper limb northward transport entering the Irminger Sea across OSNAP East (Table 1; see IG & IC), since the majority of water flowing northward does so in the lower limb of the MOC (de Jong et al., 2020). The equal magnitudes of the upper limb transports entering the Irminger Sea northward (IG & IC) and leaving the Iceland Basin southward via the East Reykjanes Ridge Current (ERRC) in Table 1 is explained by the rapid anticyclonic recirculation of water south of the OSNAP East section. Along the western boundary, the isopycnal of maximum overturning slopes steeply with distance offshore during spring, decreasing the cross-sectional area over which southward flow can contribute to the upper limb of the MOC at OSNAP East. Thus, since less upper limb southward transport is available in the EGC ( $-2.1 \text{ Sv}$ , Table 1) to compensate for the stronger northward transport above  $\sigma_{MOC}$  in the NAC ( $20.7 \text{ Sv}$ , Table 1), the MOC reaches a seasonal maximum in spring.

A contrasting density structure is found in autumn, when Figure 4b shows that surface heating through summer has restored the stratification in the upper Irminger Sea. This agrees closely with the recent observations of de Jong et al. (2020), who found the lowest monthly mean density along OSNAP East during October. Since the depth of  $\sigma_{MOC}$  in Figure 4b exceeds 100 m throughout the entire Irminger Basin, there is a larger northward upper limb transport in the Irminger Gyre and the Irminger Current ( $4.2 \text{ Sv}$ ). However, this is more than compensated for by the vertical migration of the isopycnal of maximum overturning offshore of the East Greenland shelfbreak, which enables water flowing southward in the upper 200 m of the EGC to be included within the lighter MOC upper limb ( $\sigma_{MOC} = 27.50 \text{ kg m}^{-3}$  in October) as recently observed by Le Bras et al. (2020). This, in conjunction with the weaker transport of warm, saline water flowing northward in the NAC (a change of  $-1.4 \text{ Sv}$ ), is therefore responsible for the MOC seasonal minimum in October.

In contrast with the conclusion of Wang et al. (2021), we do not find that the seasonal cycle of the MOC can be accounted for by changes in the density structure of the western Irminger Basin alone. Rather, we propose that seasonal variations in the velocity field of the upper EGC act in conjunction with migrations of  $\sigma_{MOC}$  to drive the seasonality of Eulerian overturning at OSNAP East. To demonstrate this, we consider the Lagrangian trajectories of water parcels recirculating exclusively within the upper 250 m of the Irminger Sea. Following Våge et al. (2011), and supported by our simulated time-mean current structure, we define a fixed boundary located 500 km from Cape Farewell (see Fig. 3) to differentiate between the cyclonic circulation pathways of the Irminger Gyre (*IG*), recirculating within the basin interior, and the Irminger Current (*IC*), positioned on the western flank of the Reykjanes Ridge. Figure 5a shows a strong seasonal signal in the median amount of time water parcels spend north of OSNAP East; recirculation times are longest when water parcels flow northward across OSNAP East during winter and are shortest when they cross the section during summer. For the upper *IC* pathway, this amounts to water parcels typically spending 8 months circulating along the boundary current following initialisation in February compared with only 6 months when initialised in August (Fig. 5a).

Critically, it is the decrease in upper *IG* and *IC* recirculation times between February-May (Fig. 5a) which contributes to the seasonality of Eulerian overturning at OSNAP East. This is because the reduction in the recirculation times of water parcels crossing OSNAP East northwards in the upper *IC* during spring produces a convergence of water parcels flowing southward

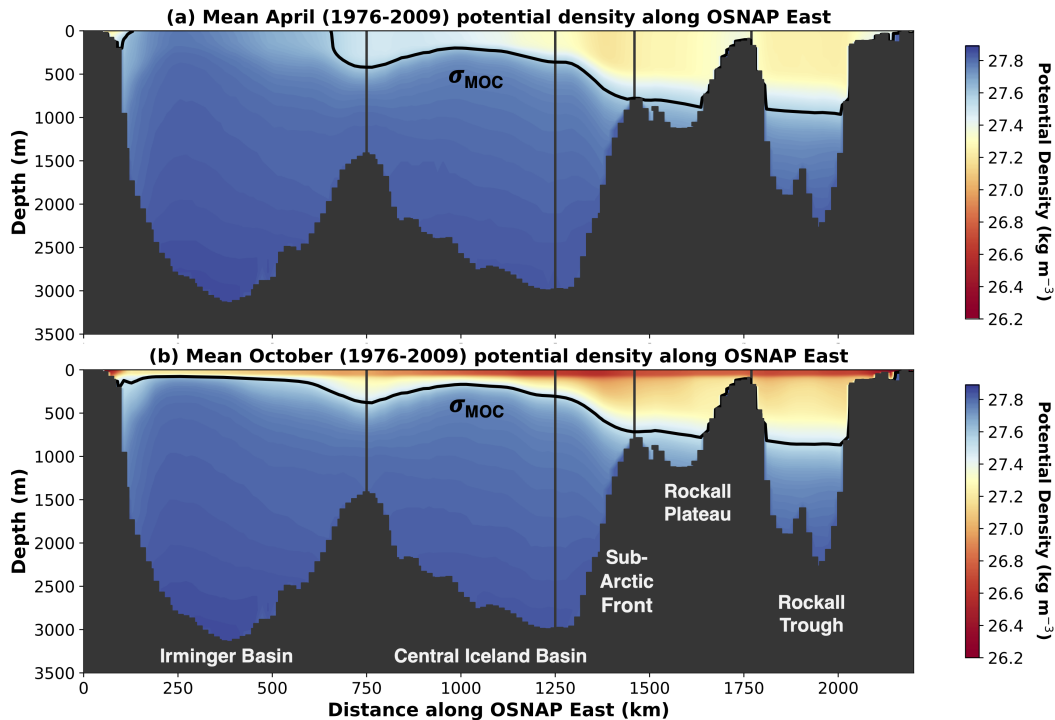


**Figure 4.** Mean potential density along the model-defined OSNAP East section in (a) April and (b) October overlaid by the corresponding mean isopycnal of maximum Eulerian overturning (April:  $\sigma_{MOC} = 27.57 \text{ kg m}^{-3}$ , October:  $\sigma_{MOC} = 27.50 \text{ kg m}^{-3}$ ), denoting the seasonal interface between the upper and lower limbs of the MOC.

in the upper EGC during autumn. The strongest convergence occurs in October, consistent with the observed intensification of the upper EGC at OSNAP East during autumn (Le Bras et al., 2018; Pacini et al., 2020), and amounts to a 1.0 Sv negative anomaly in the full-depth transport of the EGC. While the magnitude of this transport anomaly remains small compared with the typical magnitude of the EGC in this simulation (31.0 Sv), its surface-intensified nature has disproportionate consequences for the strength of the MOC at OSNAP East. Figure 5a shows that the convergence of upper Irminger Sea water parcels within the EGC occurs almost exclusively within the upper limb of the MOC. Thus, by acting in concert with the deepening of  $\sigma_{MOC}$  during late-summer and autumn (Fig. 4b), the convergence of upper *IG* and *IC* water parcels within the boundary current can explain 2.6 Sv of the 2.8 Sv increase in the upper limb EGC southward transport between April and October, accounting for almost two-thirds of the amplitude of the MOC seasonal cycle at OSNAP East (4.2 Sv).

Previous studies have highlighted the close relationship between seasonal variations in the large-scale circulation of the Irminger Sea and wind-stress forcing acting over the basin (Daniault et al., 2011a, b; Le Bras et al., 2018). To determine whether local wind-stress forcing can account for the seasonality of water parcel recirculation times in the upper Irminger Sea, we next compare the character of upper *IC* trajectories flowing northward across OSNAP East in February and August, corresponding to the longest and shortest recirculation times, respectively. Figure 5b shows that the longer median recirculation times of

upper *IC* water parcels flowing northward across OSNAP East in February is due to their slower advection along the boundary current through spring-summer. The weakening of the boundary current is explained by the springtime spin-down of the gyre circulation owing to the decrease in wind-stress curl acting over the Irminger Sea (Daniault et al., 2011a). In addition to their  
380 slower recirculation times along the boundary current, water parcels flowing northward in February are more likely to be entrained into slower circulation pathways in the basin interior, resulting in a longer tail in the distribution of recirculation times in Figure 5c. The shorter recirculation times exhibited by upper *IC* water parcels flowing northward in August results from the autumn-wintertime spin-up of the gyre during their recirculation north of OSNAP East. Figure 5b shows that water parcels flowing northward in August experience especially fast advection within the EGC, where the strongest north-easterly  
385 winds act along-stream. This is consistent with the study of Le Bras et al. (2018), who found that seasonal variations in the wind-stress curl, and by extension the EGC transport, are largely determined by changes in the local wind stress field acting along the East Greenland coast.



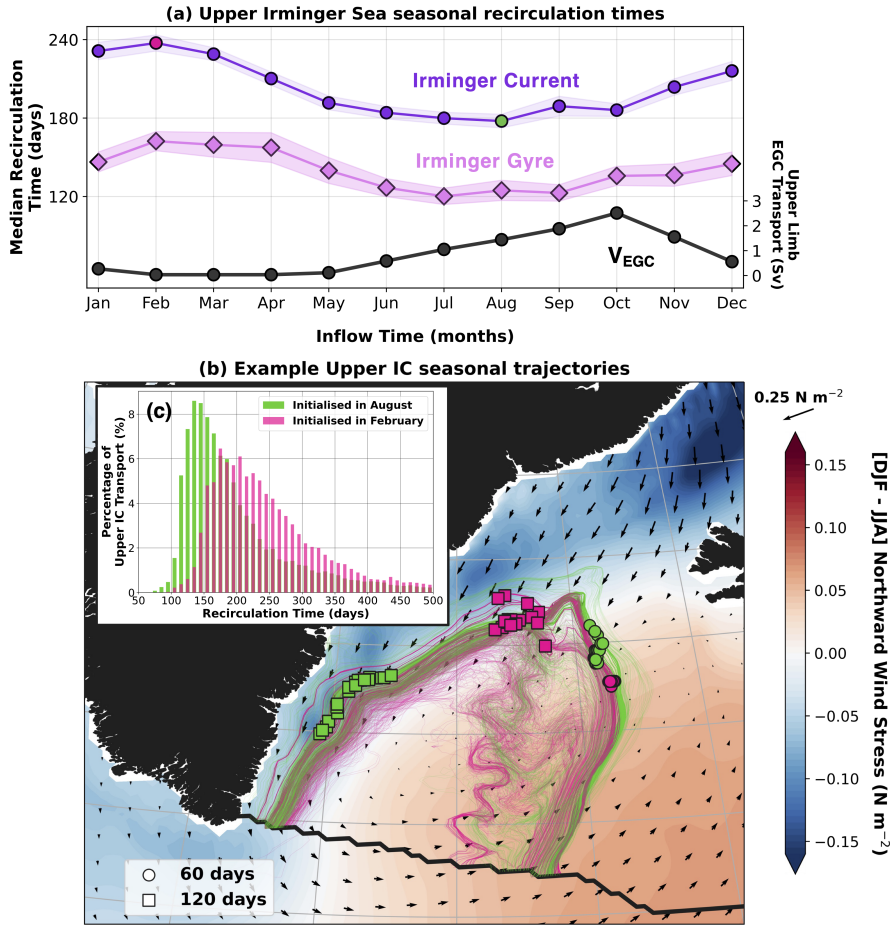


**Figure 5.** (a) Seasonal cycle of median recirculation times north of the model-defined OSNAP East section for water parcels initialised in the upper 250 m of the Irminger Current (IC, purple) and Irminger Gyre (IG, pink) pathways. The total volume transport of upper Irminger Sea water parcels flowing southward in the EGC within the upper limb (i.e., above  $\sigma_{MOC}$ ) is given by the solid black line ( $V_{EGC}$ ). Note that, unlike the water parcel recirculation times (purple and pink), the EGC volume transports (black) are plotted according to the month during which they cross OSNAP East southward in the EGC. (b) Example water parcel trajectories flowing northward in the upper 250m of the Irminger Current during February (pink) and August (green) 2000. The associated median recirculation times are also coloured accordingly in a). Way point markers show the locations of water parcels remaining within the boundary current at 60- (circles) and 120-days (squares) following initialisation. Trajectories are superimposed on filled contours of the difference between the mean winter (DJF) and summer (JJA) northward component of the wind stress fields calculated between 1976-2015. The time-mean wind stress field (1976-2015) is shown by the overlying vectors included at the centre of every 4<sup>th</sup> model grid cell. (c) Distributions of upper IC recirculation times determined from all of the water parcels flowing northward across OSNAP East during February (pink) and August (green) between 1976-2008 (i.e., 33 initialisations for each month).

390 It is important to emphasise that the relationship we have determined between wind-stress forcing and seasonal Eulerian overturning variability at OSNAP East may not be applicable throughout the entire SPNA. For example, Wang et al. (2021) showed that dramatic seasonal variations in wind-stress curl over the Labrador Sea do not translate into overturning seasonality, given that northward and southward boundary current transports across OSNAP West vary synchronously and thus act to compensate one another on seasonal timescales. This suggests that the larger basin geometry of the eastern SPNA plays an integral role in enabling seasonal wind-stress forcing to project onto the seasonal overturning variability recorded at OSNAP East.

## 395 4 Seasonal overturning variability: A Lagrangian perspective

### 4.1 Seasonal Lagrangian overturning at OSNAP East

The Lagrangian overturning framework provides us with an alternative view of the overturning variability at OSNAP East on seasonal timescales. Whereas the Eulerian streamfunction integrates the meridional transports across OSNAP East in density-space at a given point in time, the LOF measures the net diapycnal transformation that the total northward transport arriving at OSNAP East will go on to experience during its recirculation within the eastern SPGeSPG. As such, the meridional transports comprising the LOF belong to a single collection of water parcels (sharing a common inflow time), whereas the Eulerian streamfunction includes two unrelated collections of water parcels flowing northwards and southwards, respectively. We should therefore consider the LOF to be a complementary measure of the overturning at OSNAP East, which preserves knowledge of water parcel identity at the expense of integrating across water parcel recirculation times which can extend from days to years explicitly accounts for both the transformation and subsequent export of water masses within the eSPG by preserving knowledge of water parcel identity.

Figure 36a presents the strength of the LMOC within the eastern SPG Lagrangian overturning within the eSPG between 1976 and 2008, consistent with our earlier Eulerian analysis (Fig. 2a). The smaller magnitude of Lagrangian overturning in Figure 6a compared with the Eulerian overturning shown in Figure 2a is due to the exclusion of water parcels which are overturned north of the Greenland-Scotland Ridge from our analysis. We find that, on average, 8.9 Sv of transport  $\pm 2.2$  Sv of water flowing northwards across OSNAP East is transformed-transferred from the upper to the lower limb south of the Greenland-Scotland Ridge. Importantly, this of the LMOC within the Iceland and Irminger basins. This transformation is stronger than the mean eastern SPG-Lagrangian overturning found in ?Tooth et al. (2023), because here we compute the average of the maximum Lagrangian overturning each month as opposed to taking the maximum of the mean LOF as in ?. We attribute the remaining 6.5 Sv (15.4 Sv - 8.9 Sv) of Tooth et al. (2023). To highlight the fidelity of the simulated Lagrangian overturning at OSNAP East to water parcels which are transformed north of the Greenland-Scotland Ridge before returning via the deep pathways of Nordic Seas overflows. Although we do not resolve the overturning pathways of the Nordic Seas overflows in this Lagrangian experiment, the close correspondence between the month-to-month Lagrangian overturning variability of the eastern SPG (SD =  $\pm 2.2$  Sv) shown in Figure 3a and the total month-to-month variability of the MOC (SD =  $\pm 2.7$  Sv) underscores the dominant contribution made by the eastern SPG to intra-annual overturning variability at OSNAP East, we note the good

agreement between the simulated mean strength of the LMOC and observed estimates of 7.6-10.2 Sv of overturning within the Iceland and Irminger basins (Chafik and Rossby, 2019; Petit et al., 2020; Sarafanov et al., 2012).

In contrast with the seasonality of the Eulerian ~~MOC~~overturning at OSNAP East, the seasonal cycle of Lagrangian overturning ~~within the eastern SPG in Figure 6b~~ shows a steady increase from a minimum of 6.4 Sv in May to a maximum of 11.5 Sv in November. While the phase difference between the seasonal cycles of the MOC and the LMOC may initially appear counter-intuitive, recall that the strength of the Lagrangian overturning ~~in Figure 3b~~ quantifies how much of the total northward transport ~~initialised along OSNAP East each~~ flowing north across OSNAP East in any given month is transformed from the upper to the lower limb in the ~~Irminger and Iceland-Rockall Basins~~Iceland and Irminger basins. Interestingly, the seasonal cycle of the LMOC strength ~~corresponds closely~~ is closely correlated with the seasonality of both  $\sigma_{LMOC}$  (Fig. 6b:  $r = -0.85$ ,  $p < 0.01$ ) and  $\sigma_{MOC}$  (see Figs Fig. 2b and 3b:  $r = -0.86$ ,  $p < 0.01$ ), suggesting that the potential density of upper limb water parcels on flowing northward across OSNAP East is an important indicator of their future contribution to ~~the overturning~~ overturning seasonality north of the section. This ~~relationship can also be seen in Figure 3e, which is in marked contrast to the seasonal cycle of the Eulerian MOC, which implies that the coldest and densest upper limb waters flowing northward across OSNAP East in April lead to a maximum in overturning strength.~~

To better understand the relationship between the composition of the upper limb and the strength of Lagrangian overturning, Figure 6c shows how the LOF evolves over the duration of the mean seasonal cycle. Here, we find that the maximum of the LMOC in November occurs when the largest number of, for water parcels flowing north in November, occurs when relatively light upper limb water parcels ~~are able to integrate~~ experience sufficient wintertime surface buoyancy loss to enter the lower limb before returning to OSNAP East. Meanwhile, ~~in May, we find that~~ denser upper limb ~~waters~~water parcels arriving at OSNAP East in May, previously transformed by wintertime cooling ~~in the NAC~~, experience substantial summertime buoyancy gain north of OSNAP East to become lighter downstream. This negative diapycnal transformation ~~manifests in Figure 3e through both~~ is captured in the pronounced region of negative Lagrangian overturning between  $26.8-27.2 \text{ kg m}^{-3}$  ~~and the seasonal minimum of the LMOC in Figure 6c and results in the weakest seasonal volume flux into the lower limb.~~

The seasonal cycle of Lagrangian overturning ~~within the eastern SPG at OSNAP East~~ therefore reflects the seasonality of the surface-forced water mass transformation within the ~~Irminger and Iceland-Rockall Basins north of OSNAP East~~Iceland and Irminger basins. The strengthening of the LMOC for water parcels crossing OSNAP East in summer-autumn corresponds to increasing ~~diapycnal transformation volume flux~~ across  $\sigma_{LMOC}$ , owing to intense surface buoyancy loss along ~~particle~~ water parcel trajectories during the ensuing winter. Meanwhile, the weakening of the LMOC for parcels crossing OSNAP East through winter-spring reflects a decreasing volume flux into the lower limb as water parcels in the upper limb gain buoyancy along their trajectories during the ensuing summer.

~~Lagrangian overturning variability of the eastern SPG at OSNAP East. (a) Monthly maximum of the Lagrangian Overturning Function in density-space (computed from the subset of particles initialised on the inflow across OSNAP East that recirculate south of the Greenland-Scotland Ridge, grey line) and 1-year annual running mean (bold black line) overlaid for 1976-2008. (b) Mean seasonal cycles of the maximum of the Lagrangian Overturning Function and the isopycnal of maximum Lagrangian overturning ( $\sigma_{LMOC}$ ) computed from monthly composites. Shading represents  $\pm 1$  standard error of the monthly estimates. (c)~~

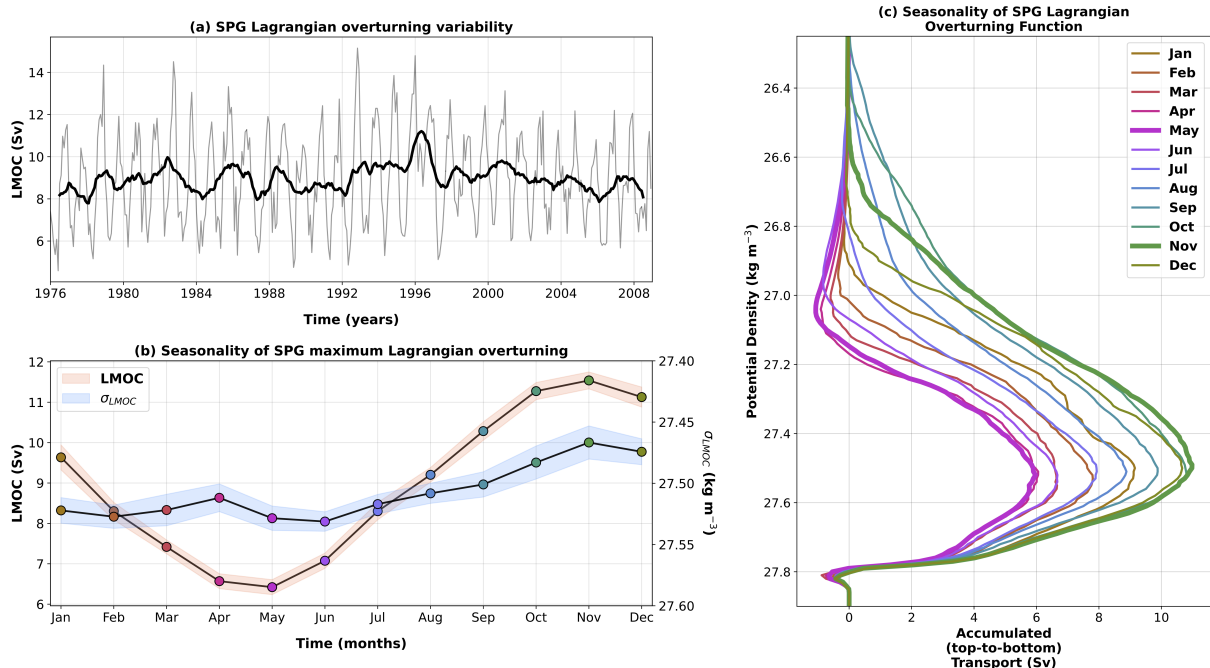


**Figure 6.** Lagrangian overturning variability of the eSPG at the model-defined OSNAP East section. The LOF for any given month describes the subsequent transformation of recirculating water parcels crossing the OSNAP East section northward in that month. (a) Monthly maximum of the Lagrangian Overturning Function in density-space (computed from the subset of particles initialised on the inflow across OSNAP East that recirculate south of the Greenland-Scotland Ridge, grey line) and 1 year annual running mean (bold black line) overlaid for 1976-2008. (b) Mean seasonal cycles of the maximum of the Lagrangian Overturning Function and the isopycnal of maximum Lagrangian overturning ( $\sigma_{LMOc}$ ) computed from monthly composites. Shading represents  $\pm 1$  standard error of the monthly estimates. (c) Monthly composites of the Lagrangian Overturning Function calculated in discrete density-space (bin width is  $0.01 \text{ kg m}^{-3}$ ); maximum (November) and minimum (May) months in the LMOc seasonal cycle are included in bold.

Monthly composites of the Lagrangian Overturning Function calculated in discrete density-space (bin width is  $0.01 \text{ kg m}^{-3}$ ); maximum (November) and minimum (May) months in the LMOc seasonal cycle are included in bold.

## 5 Timescales and origins of seasonal Lagrangian overturning

### 4.1 Timescales and origins of seasonal Lagrangian overturning

460 We have demonstrated that variations in the Lagrangian overturning evaluated a close phase relationship exists between the seasonal cycle of Lagrangian overturning at OSNAP East are most pronounced on seasonal timescales and the seasonality of surface buoyancy forcing over the Iceland and Irminger basins. However, we have yet to establish why the magnitude of seasonal variability (SD of LMOc seasonal cycle =  $\pm 2.1 \text{ Sv}$ ) remains small compared with the mean strength of overturning

(LMOC = 8.9 Sv), suggesting that the majority of water parcels flowing northwards across OSNAP East in the upper limb are transferred into the lower limb before returning to the section (large seasonal cycle of surface buoyancy-driven transformation (Xu et al., 2018b; Petit et al., 2020)). Since wintertime surface buoyancy loss greatly exceeds summertime buoyancy gain over the eastern-SPG eSPG (Xu et al., 2018b), the mean strength of the LMOC is governed by the fraction of upper limb water parcels which fail to return to OSNAP East before the onset of winter and therefore integrate experience sufficient surface buoyancy loss to be transferred into the lower limb during their recirculation. In contrast, the The seasonality of Lagrangian overturning is instead determined by rapidly recirculating water parcels whose diapycnal transformation north of OSNAP East is dependent on the time of year that they arrive at the section. The minimum of the LMOC seasonal cycle (Fig. 3b) is due to the coldest upper limb water parcels arriving at the section in spring, which experience summertime warming before returning to OSNAP East prior to the onset of wintertime densification. The maximum of the LMOC seasonal cycle, corresponding to the largest volume flux into the lower limb, is due to the warmest upper limb water parcels flowing northwards across the section in autumn, which experience the largest wintertime surface buoyancy loss downstream. This qualitative description of seasonal overturning variability raises two important questions. Firstly, what is the maximum amount of time a water parcel can spend north of OSNAP East and still contribute to the seasonal cycle of Lagrangian overturning? Secondly, are the To better distinguish between the origins and advective timescales of water parcels responsible for seasonal variability sourced from distinct inflow regions along OSNAP East when compared with those contributing substantially to the mean state of overturning? To address these questions, we the mean strength and seasonality of Lagrangian overturning at OSNAP East, we next decompose the LOF according to both the time water parcels spend north of OSNAP East (herein referred to as the water parcel recirculation time,  $\tau$ ) and the distance from the East Greenland coast that water parcels flow northward across the section (Fig. 47).

Figure 47a presents the proportion of the mean strength of Lagrangian overturning and amplitude of the seasonal cycle (difference between November-May LMOC monthly composites) accumulated as a function of the time water parcels spend north of OSNAP East ( $\tau$ ). We find that the entire LMOC seasonal cycle and 25% of the mean strength of Lagrangian overturning can be explained by water parcels which spend less than 8.5 months recirculating within the eastern-SPG eSPG. Interestingly, the absence of any further accumulation of seasonal Lagrangian overturning variability after 8.5 months following northward inflow across OSNAP East implies that, irrespective of its time of arrival, once a water parcel has experienced wintertime surface buoyancy loss it can no longer imprint onto the seasonal cycle of Lagrangian overturning. Thus, the remaining 75% of the mean LMOC strength volume flux into the LMOC lower limb is accounted for by water parcels which spend between 8.5 months and 5 years recirculating within the eastern-SPG eSPG, and experience at least one winter north of OSNAP East. We should note, however, that the accumulation of the mean Lagrangian overturning is not linear over this period; 91% of the volume flux from the upper to the lower limb is owed to water parcels recirculating in 2 years or less (Fig. 4a).

To understand how the recirculation time of a water parcel is related to its inflow position along OSNAP East, we next calculate the average recirculation time of water parcels within the eastern-SPG eSPG as a function of their northward crossing locations along the section. Figure 47b indicates that, on average, the recirculation times of the major upper ocean currents intercepted by OSNAP East are shortest in the upper ocean and increase strongly with depth. This is consistent with observa-

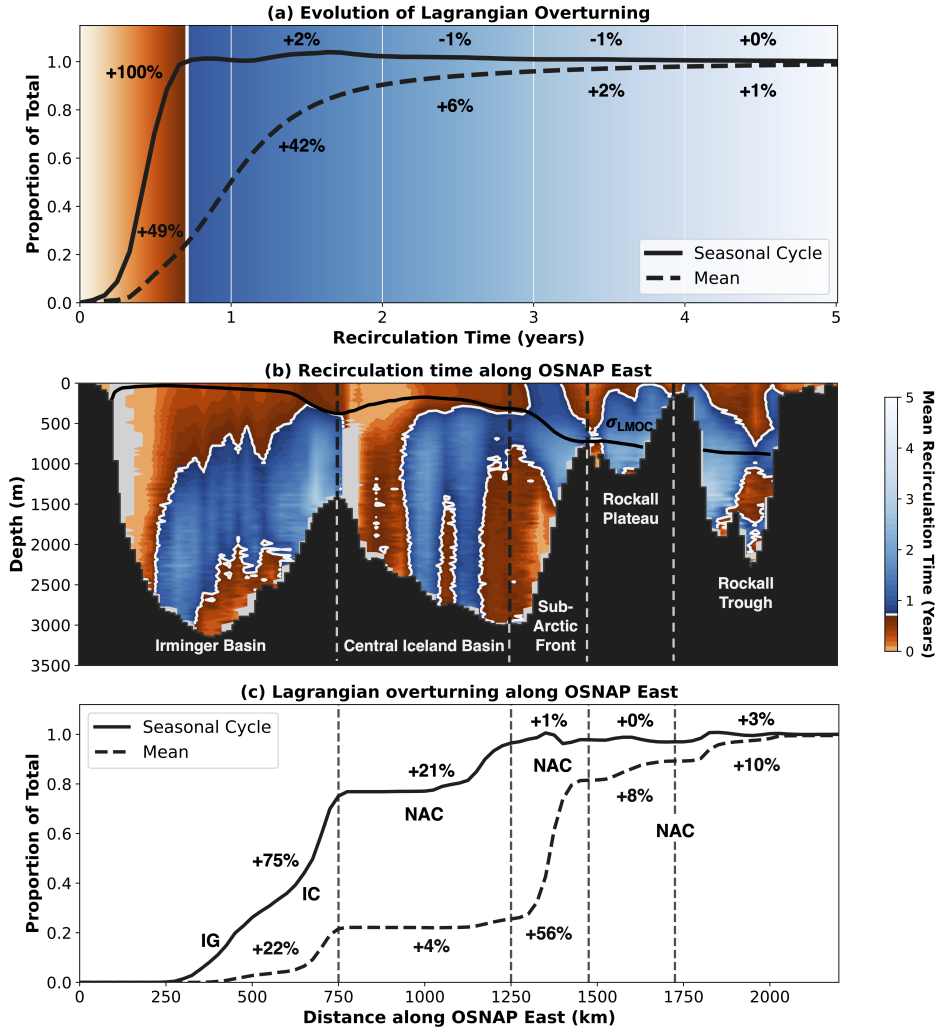


**Figure 7.** Decomposition of the mean strength and seasonality of Lagrangian overturning within the [eastern-SPG-eSPG](#) by recirculation time and distance along OSNAP East. (a) Normalised mean strength and seasonality (amplitude of the seasonal cycle calculated as November-May difference between LMOC monthly composites) of the Lagrangian overturning at  $\sigma_{LMOC}$  evaluated as a function of the time in which water parcels recirculate back to the OSNAP East section. (b) Mean recirculation time of water parcels initialised on the northward inflow across OSNAP East as a function of their initial position in  $x-z$  space, where  $x$  is the distance along the OSNAP East section (km) and  $z$  is the depth (m). All 9.8 million [eastern-SPG-eSPG](#) water parcels initialised across 396 months (1976-2008) are binned according to their initial position, before computing the mean recirculation time for each bin ( $\Delta z = 25$  m,  $\Delta x = 25$  km). [White-Grey](#) regions coincide with the major southward currents intersected by the OSNAP East array, hence no northward flowing water parcels are initialised here. (c) Normalised mean strength and seasonality of the Lagrangian overturning at  $\sigma_{LMOC}$  accumulated as a function of the distance from the East Greenland coast that water parcels flow northward across OSNAP East.



tions in the eastern SPNA, which show that northward transport is surface intensified in the NAC branches (Holliday et al., 2018; Houpert et al., 2018, 2020) and the Irminger Current (de Jong et al., 2020; Fried and de Jong, 2022) since isopycnals in the upper ocean shoal strongly westward. We attribute the short recirculation times ( $\tau \leq 8.5$  months) found in the lower limb in Figure 7b to short-lived mesoscale eddies which are partially resolved in the simulated velocity field. A prominent feature of Figure 47b is the transition from upper limb pathways which contribute to the seasonal cycle of the LMOC (orange,  $\tau \leq 8.5$  months) in the Irminger and Central Iceland Basins to longer pathways (blue,  $\tau > 8.5$  months), sourced from the central and southern NAC branches, which dominate its mean strength. Figure 47c quantifies this distinction, highlighting that 74% of the mean strength of the LMOC is due to water parcels originating from the Sub-Arctic Front and the Rockall Trough and Plateau, whereas 96% of the mean seasonal cycle of Lagrangian overturning can be explained by water parcels sourced from the Irminger and Central Iceland Basins ( $x \leq 1250$  km). ~~This finding is further supported by the recent results of Li et al. (2021a), who found that changes in the observed velocity and density fields between the East Greenland coast and the Central Iceland Basin can explain 75% of the monthly MOC variance across OSNAP East between 2014–16~~ We note that the recirculation times of water parcels flowing northward in the upper 250-m of the Central Iceland and Irminger basins also vary seasonally (see Fig. 5a), however this does not influence their contribution to the mean seasonal cycle of Lagrangian overturning.

To summarise, we have ~~identified a threshold recirculation time of 8.5 months which governs whether water parcels will contribute substantially to~~ found a clear distinction between the origins and advective timescales of water parcels responsible for the mean strength ~~of the LMOC or determine its seasonal signal and seasonality of Lagrangian overturning~~ at OSNAP East. Seasonal overturning variability is ~~sourced from the~~ associated with water crossing the section in the upper Irminger and Central Iceland Basins, where the rapid recirculation of water parcels in less than 8.5 months yields along-stream transformations which are dependent on their time of arrival at OSNAP East. Conversely, the mean strength of the LMOC is determined by water parcels, originating from the central and southern NAC branches, whose longer recirculation time ( $\tau > 8.5$  months) guarantees their diapycnal transformation into the LMOC lower limb through intense wintertime buoyancy loss.

## 5 Seasonal Lagrangian overturning pathways within the eastern SPG

### 4.1 Pathways of seasonal Lagrangian overturning

~~Decomposition of the seasonal cycle of Lagrangian overturning within the eastern SPG by circulation pathway north of OSNAP East. (a) Example water parcel trajectories illustrating each of the four circulation pathways within the eastern SPG and their respective contributions to the mean strength of Lagrangian overturning at  $\sigma_{LMOC}$ . (b) Inflow locations where water parcels are advected northward across OSNAP East classified by pathway. Water parcel volume transports for each pathway are averaged in discrete  $x-z$  space ( $\Delta z = 25$  m,  $\Delta x = 25$  km) using all 396 initialisation months before normalising by the maximum mean transport recorded across all bins (darker shading corresponds to the strongest northward transport for each pathway). (c) Seasonal cycle of the Lagrangian overturning at  $\sigma_{LMOC}$  decomposed by circulation pathway north of OSNAP East. For clarity, variations in the LMOC are presented as anomalies about the time-mean overturning determined from monthly composites of each pathway. (d) The proportion of the total diapycnal transport ( $|\Delta\sigma| > 0.01 \text{ kg m}^{-3}$ , where  $\Delta\sigma$  is the net change in potential~~

density between northward and southward crossing of OSNAP East) to have successfully recirculated back to OSNAP East as a function of the time elapsed following northward flow across the section. Coloured circles correspond to the median recirculation time of each circulation pathway.

## 535 4.2 Pathways of seasonal overturning variability

Following ~~?~~To further investigate the sources of seasonal Lagrangian overturning variability within the eSPG, we classify water parcels according to ~~four~~ five cyclonic circulation pathways defined between OSNAP East and the Greenland-Scotland Ridge. The majority of water parcels recirculate exclusively within the Iceland-Rockall ~~and Irminger Basins and are referred to as the (IcRo-IcRo) and Irminger basins (IG and IcRo-IcRo and Irm-Irm pathways, respectively (IC, see Fig. 5a-8b for regional definitions). The remaining water parcels cross the section in the NAC and flow westward across the Reykjanes Ridge before ~~crossing OSNAP East in~~ returning to OSNAP East via the East Greenland Current, which flows southward along the western boundary of the Irminger ~~Basin~~ Sea. These water parcels are subdivided into two pathways according to their inflow location along the section: the Ic-RR-IrmIc-Irm pathway comprises water parcels sourced from the central NAC branch positioned along the Sub-Arctic Front, while the Ro-RR-IrmRo-Irm pathway originates from the southern NAC branch feeding both the ~~Rockall Trough and the Rockall Plateau (Fig. 58b).~~~~

Concordant with our earlier analysis, Figure ~~5 shows a~~ 8 shows the clear distinction between the circulation pathways responsible for the seasonality of the LMOC and those governing its mean state. We find that the two pathways crossing the Reykjanes Ridge north of OSNAP East account for 70% of the mean strength of the Lagrangian overturning within the ~~eastern SPG-eSPG (Fig. 8a)~~ yet exhibit negligible variability on seasonal timescales (Fig. 58c). This is because the recirculation times of water parcels advected across the ridge north of OSNAP East consistently exceed the critical 8.5 month threshold required to be irreversibly transferred into the lower limb of the LMOC. Water parcels advected along the Ic-RR-IrmIc-Irm pathway typically experience 1.1 years (Fig. 58d) of along-stream surface buoyancy loss in order to transfer  $4.8 \pm 1.0$  Sv of water into the lower limb. ~~Water parcels flowing northward along the slower~~ As shown in Tooth et al. (2023), the slower Ro-RR-IrmRo-Irm pathway ( $\bar{\tau} = 1.7$  years) ~~form~~ forms  $1.4 \pm 0.4$  Sv of dense Icelandic Slope Water (Van Aken and De Boer, 1995; Read, 2000) by entraining Iceland Scotland Overflow Water (ISOW) in the vicinity of the Faroe Bank Channel (Fig. 58a).

Figure 58c shows that ~~water parcels recirculating exclusively within the Irminger Basin (Irm-Irm) explain 75% of the amplitude of the LMOC seasonal cycle at OSNAP East (Fig. 4). However, our use of a single Irm-Irm pathway obscures two separate pathways that circulate cyclonically within the Irminger Sea, namely the Irminger Current IC and the Irminger Gyre IG. Therefore, to isolate the Lagrangian overturning occurring along each of these pathways, we define the boundary between the IG, recirculating within the basin interior, and the seasonal cycle of Lagrangian overturning at OSNAP East is dominated by water parcels recirculating exclusively within the Irminger basin (IG + IC, positioned on the western flank of the Reykjanes Ridge, to be 500 km from Cape Farewell, following Våge et al. (2011)).~~ We find that the northward inflows to the IG ( $x \leq 500$  km) make a disproportionately large contribution to the seasonality of Lagrangian overturning the LMOC (26%) compared with their limited contribution to its mean strength (3%). Water parcels advected along the path of the IC ( $500 \text{ km} < x \leq 750$  km) explain almost half (49%) of the seasonal cycle of Lagrangian overturning whilst also accounting for approximately a fifth

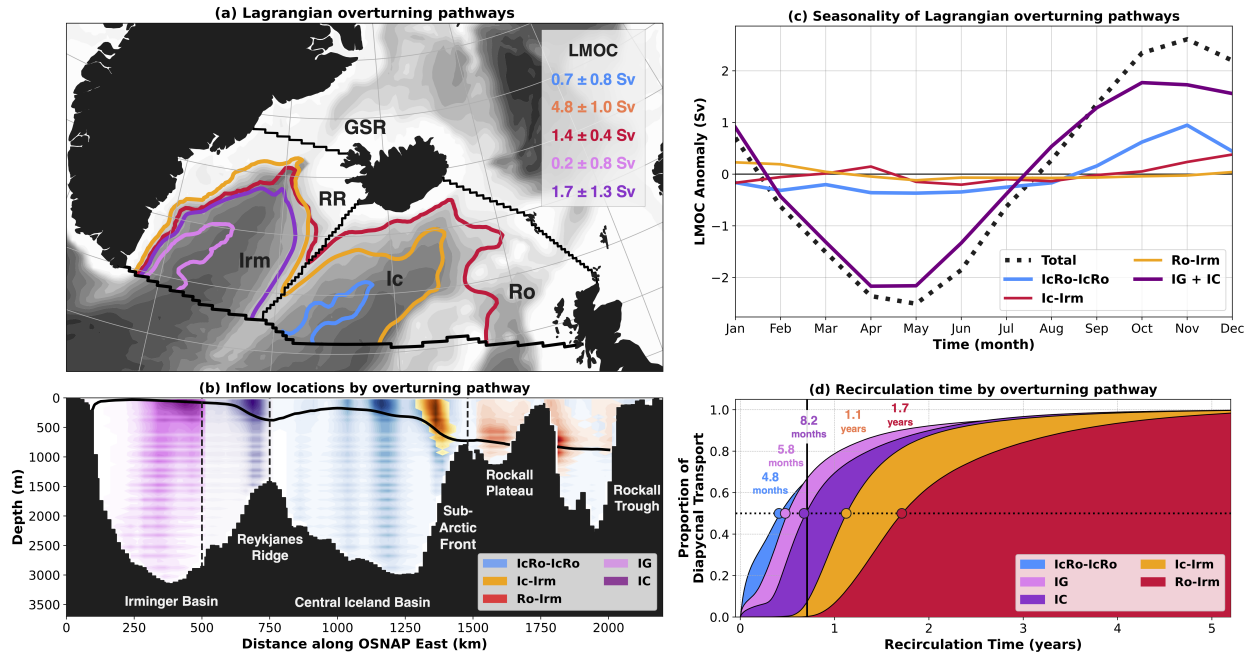


**Figure 8.** Decomposition of the seasonal cycle of Lagrangian overturning by circulation pathway north of the model-defined OSNAP East section. (a) Example water parcel trajectories illustrating each of the five circulation pathways within the eSPG and their respective contributions to the mean strength of Lagrangian overturning at  $\sigma_{LMOC}$ . (b) Inflow locations where water parcels are advected northward across OSNAP East classified by pathway. Water parcel volume transports for each pathway are averaged in discrete  $x - z$  space ( $\Delta z = 25$  m,  $\Delta x = 25$  km) using all 396 initialisation months before normalising by the maximum mean transport recorded across all bins (darker shading corresponds to the strongest northward transport for each pathway). (c) Seasonal cycle of the Lagrangian overturning at  $\sigma_{LMOC}$  decomposed by circulation pathway north of OSNAP East. For clarity, variations in the LMOC are presented as anomalies about the time-mean overturning determined from monthly composites of each pathway. (d) The proportion of the total diapycnal transport ( $|\Delta\sigma| > 0.01$  kg m<sup>-3</sup>, where  $\Delta\sigma$  is the net change in potential density between northward and southward crossing of OSNAP East) to have successfully recirculated back to OSNAP East as a function of the time elapsed following northward flow across the section. Coloured circles correspond to the median recirculation time of each circulation pathway.

(19%) of the mean volume flux across  $\sigma_{LMOC}$  into the lower limb. The larger overturning-associated-with-contribution of the IC pathway to the mean Lagrangian overturning is explained by Figure 58d, which shows that water parcels typically spend 8.2 months recirculating within the IC compared with only 5.8 months within the IG. Since the median recirculation time of the IC pathway is comparable to the 8.5-month threshold required to avoid wintertime densification north of OSNAP East intense wintertime surface buoyancy loss, it follows that approximately half of all water parcels advected along the boundary current of the Irminger Sea will be transformed across  $\sigma_{LMOC}$  transferred into the lower limb north of OSNAP East.

Although ~~watermass~~ diapycnal transformation along the *IcRo-IcRo* pathway accounts for only a quarter of the ~~LMOC~~ seasonal cycle ~~seasonal cycle of Lagrangian overturning~~ at OSNAP East, Figure 58c highlights its critical role in establishing the timing of the ~~November maximum in the seasonal cycle of Lagrangian overturning~~ seasonal maximum of the LMOC.  
575 Notably, it is the rapid recirculation of water parcels from the northern NAC branch to the ~~East Reykjanes Ridge Current (ERRC)~~ ERRC within 4.8 months that dominates seasonal overturning variability along this pathway. Figure 58c shows that the largest volume flux into the lower limb of the LMOC occurs ~~in November when for water flowing north in November~~ because then *IcRo-IcRo* water parcels ~~can integrate experience~~ the greatest surface buoyancy loss throughout the ensuing winter spent north of OSNAP East. This is consistent with the results of de Boisséson et al. (2010), who ~~calculated~~ found the  
580 strongest net heat loss over the Iceland Basin ~~basin~~ between November and February. ~~In contrast, a weak negative volume flux (directed from the lower to the upper limb) is found when *IcRo-IcRo* water parcels flow northward between January-August. This corresponds to the obduction of cold, fresh subpolar water across the isopycnal of maximum Lagrangian overturning within the Central Iceland Basin. Brambilla et al. (2008) attributed such negative diapycnal transformation to divergence along the northern NAC branch, which induces upwelling and hence mixing with warm, saline subpolar mode waters in the mixed~~  
585 ~~layer.~~

## 4.2 Transformation along seasonal overturning pathways

To understand how seasonal Lagrangian overturning variability results from diapycnal transformation along water parcel trajectories, we next calculate the net potential density change of water parcels between northward and southward crossings of OSNAP East,  $\Delta\sigma$ , as a function of their inflow location along the section. Figure 69a-b highlights the striking disparity between the  
590 net diapycnal transformation of water parcels flowing northward in the upper 250 m of the Irminger and Central Iceland ~~Basins~~ basins during May (lightening) and November (densification). We find that ~~the largest~~ large negative diapycnal transformations occur along water parcel trajectories sourced from the upper 100m of the *IG* and the Central Iceland Basin (*IcRo-IcRo*) in May, ~~corresponding to the minimum of the LMOC seasonal cycle. When the LMOC reaches its maximum in November~~ consistent  
595 with the pronounced region of negative Lagrangian overturning in Figure 6c. In contrast, water parcels ~~originating from the~~ upper 250 m of the *IC* flowing northward into the upper Irminger and Central Iceland basins in November undergo strong positive diapycnal transformation ~~, consistent with the expansion of the upper limb through summertime restratification. In contrast, water parcels sourced from the upper kilometer of central and southern branches of the NAC exhibit densification whatever time of year they flow north since they are guaranteed to experience at least one winter north of OSNAP East during their recirculation.~~ north of OSNAP East, and hence are responsible for the largest seasonal volume flux into the LMOC lower  
600 limb.

Since water parcels recirculating cyclonically along the boundary current of the Irminger Sea typically spend an additional 2.4 months north of OSNAP East compared with those circulating in the interior of the Irminger and Central Iceland ~~Basins~~ basins (Fig. 58), we next explore how the character of seasonal ~~water mass~~ watermass transformation differs along boundary and interior pathways within the ~~eastern SPGe~~ SPGe. We focus our analysis on the water parcels circulating  
605 in the upper 250 m of the Irminger Sea (pink and purple boxes in Figs. 9a-b), since these collectively account for three

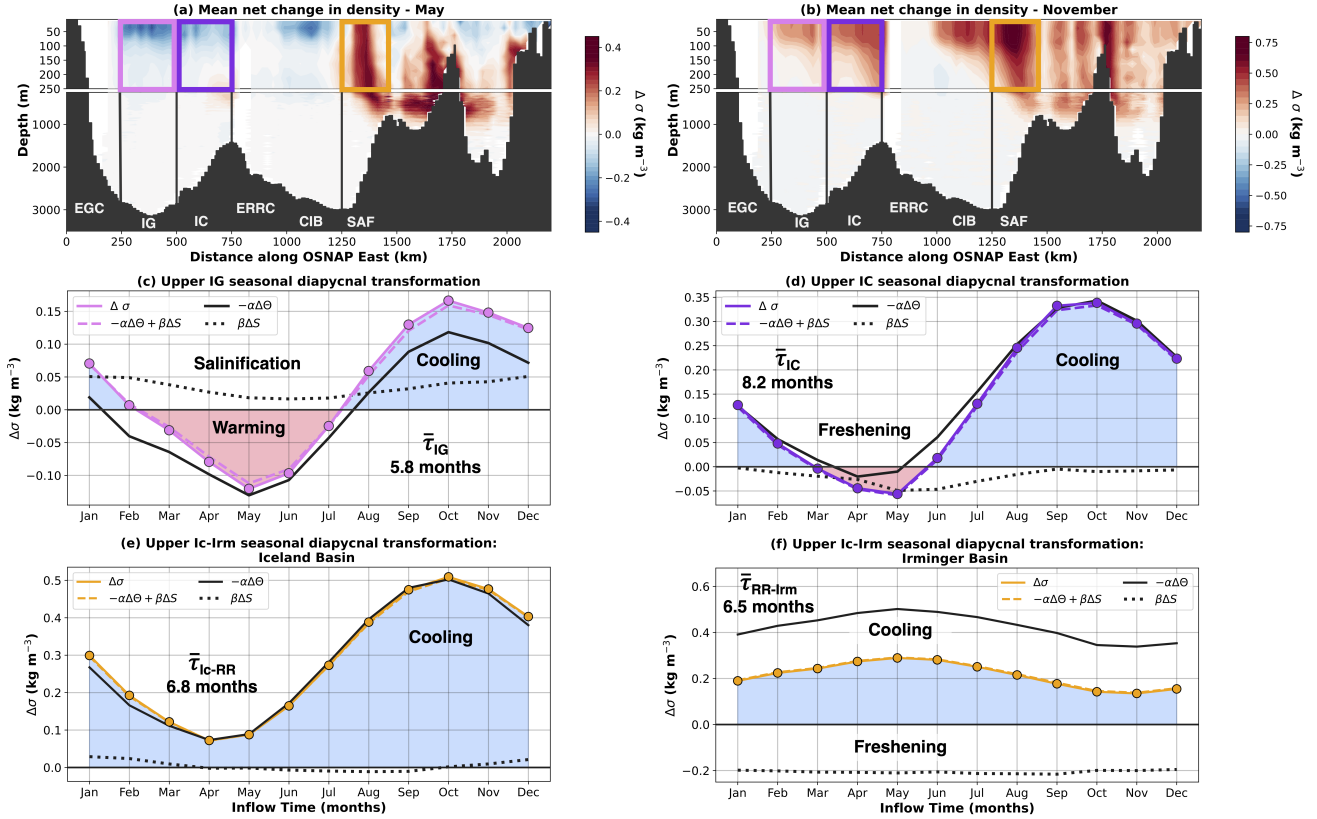


**Figure 9.** (a) Mean net change in potential density of water parcels flowing northward across OSNAP East in May as a function of their inflow location along OSNAP East. The net change in potential density,  $\Delta\sigma$  ( $\text{kg m}^{-3}$ ), between northward and southward crossings of OSNAP East is computed for each recirculating water parcel before averaging in discrete  $x-z$  space ( $\Delta z = 25$  m,  $x = 25$  km). (b) Same as (a) for water parcels flowing northward in November. Vertical solid lines correspond to the geographical limits of the major currents intercepted along the section. Boxes included in the upper 250 m define the upper *IG* (pink), *IC* (purple), *IcRo-IcRo* (blue) and *Ic-RR-Irm Ic-Irm* (orange) pathways. (c, d) Mean seasonal cycles of transport-weighted mean potential density on inflow (circular markers) and outflow (square markers) crossing of OSNAP East for the upper (c) *IG* and (d) *IC* pathways. (e, f) Mean seasonal cycle of transport-weighted mean net change in potential density and contributions from diathermal ( $\Delta\theta$ , black solid line) and diahaline ( $\Delta S$ , black dotted line) components for the upper (e) *IG* and (f) *IC* pathways. (e, f) Same as (c, d) for the *Ic-Irm* pathway once divided into two successive diapycnal transformations in the Iceland (e, *Ic-RR*) and Irminger basins (f, *RR-Irm*) using water parcel properties on crossing the Reykjanes Ridge (RR) north of OSNAP East.

quarters of the seasonal cycle of Lagrangian overturning at OSNAP East. To compare the boundary and interior modes of seasonal overturning variability, Figure 6c-d presents the transport-weighted mean potential density of upper *IG* (pink box in Fig. 6a-b) and upper *IC* (purple box in Fig. 6a-b) water parcels on their northward (*IG/IC* inflow) and subsequent southward (*EGC* outflow) crossings of the OSNAP East section. We find the densest water flowing northward in both the

610 upper **IG** and upper **IC** in April, consistent with the occurrence of the deepest mixed layers and the outcropping of  $\sigma_{LMOC}$   
following wintertime deep convection (de Jong et al., 2012; de Jong and de Steur, 2016; Piron et al., 2016). The lightest water  
parcels arrive in the upper 250 m of the Irminger Sea during September when upper ocean stratification is strongest following  
summertime heating. Despite the similar seasonality in their mean potential density on northward inflow, upper **IG** water  
parcels are consistently denser than those initialised in the upper **IC** (Fig. 6e-d) owing to their convective origins in the Labrador  
615 Sea interior (Lavender et al., 2000; Chafik et al., 2022). Moreover, upper **IG** water parcels exhibit a much narrower potential  
density range ( $27.52 - 27.68 \text{ kg m}^{-3}$ ) on southward outflow compared with those recirculating along the upper **IC** pathway  
( $27.48 - 27.59 \text{ kg m}^{-3}$ ). This is because the longer recirculation time of the upper **IC** pathway ( $\bar{\tau} = 6.2$  months) allows water  
parcels to undergo greater surface buoyancy loss along the boundary current, thereby damping the seasonality of their water  
mass properties on inflow. The additional time upper **IC** water parcels spend north of OSNAP East is also reflected by the  
620 shorter 2-month window (April-May in Fig. 6d) during which negative diapycnal transformation can occur, compared with the  
5-month window (March-July in Fig. 6e) for the rapidly recirculating upper **IG** pathway ( $\bar{\tau} = 3.8$  months).

(Fig. 7c). To determine the relative importance of temperature and salinity changes along boundary and interior pathways,  
we further decompose the net diapycnal transformation ( $\Delta\sigma$ ) north of OSNAP East into diathermal and diahaline components.  
We approximate  $\Delta\sigma$  using a linearised form of the equation of state following the integral approach of Tamsitt et al. (2018):

$$625 \quad \Delta\sigma \approx -\alpha(\bar{\theta}, \bar{S})\Delta\theta + \beta(\bar{\theta}, \bar{S})\Delta S, \quad (3)$$

where  $\theta$  denotes potential temperature,  $S$  denotes salinity,  $\alpha$  represents the thermal expansion coefficient, and  $\beta$  represents  
the haline contraction coefficient. The values of  $\bar{\theta}$  and  $\bar{S}$  correspond to the average potential temperature and salinity of a water  
parcel on its northward and southward crossings of OSNAP East.

630 ~~Figures 6e-f shows close~~ To validate our approximation, Figures 9c-d show strong agreement between the seasonal cycles  
of net diapycnal transformation (pink/purple solid line) along the upper **IG/IC** pathways and its reconstruction, given by the  
sum of diathermal ( $-\alpha\Delta\theta$ ) and diahaline ( $\beta\Delta S$ ) components (pink/purple dashed line).

Consistent with the strong seasonality of surface heat fluxes over the Irminger Basin (de Jong and de Steur, 2016; Piron et al.,  
2016), we find that the seasonal cycle of diapycnal transformation along both boundary and interior pathways is dominated by  
diathermal transformation along water parcel trajectories. ~~In contrast, along-stream diahaline transformations play opposing~~  
635 ~~roles along the~~ initialised in the upper 250 m. Yet, despite the similar seasonality in their mean potential density on northward  
inflow, upper **IG** and water parcels exhibit a much broader potential density range ( $27.52 - 27.68 \text{ kg m}^{-3}$ ; Fig. A1b) on  
southward outflow compared with those recirculating along the upper **IC** pathways. Figure 6e shows that pathway ( $27.48 -$   
 $27.59 \text{ kg m}^{-3}$ ; Fig. A1c). This is because the longer recirculation time of the upper **IC** pathway ( $\bar{\tau} = 6.2$  months) allows  
water parcels to experience a greater surface-forced diathermal transformation along the boundary current (Fig. 9d), thereby  
640 damping the seasonality of their water mass properties on inflow. The additional time upper **IC** water parcels spend north of  
OSNAP East is also reflected by the shorter 2-month window (April-May in Fig. 9d) during which water parcels flowing north



subsequently experience negative diapycnal transformation, compared with the 5-month window (March-July in Fig. 9c) for the rapidly recirculating upper *IG* pathway ( $\bar{\tau} = 3.8$  months).

645 Figures 9c-d highlight the opposing roles of along-stream diahaline transformation along boundary and interior pathways in the upper Irminger Sea. We find that upper *IG* water parcels rapidly recirculating in the interior of the Irminger Basin basin experience year-round salinification north of OSNAP East (Fig. 9c). Salinification is strongest when water parcels are initialised flow north across the section during winter, suggesting that lateral mixing between the cold, fresh interior and warmer and saltier SPMWs advected along the boundary current boundary current and cold, fresh interior waters, sourced from Labrador Sea deep convection (Lavender et al., 2000; Chafik et al., 2022), is enhanced during the ensuing months. This proposition is supported by the recent observations of de Jong et al. (2020), who found that eddy kinetic energy is largest near the surface of the Irminger Current between January and April. For upper *IG* water parcels flowing northward across OSNAP East from August-January, mixing-induced salinification acts to augment along-stream densification due to intense surface heat loss over the basin interior. Although the predominant influence of boundary-interior exchange is year-round positive diahaline transformation, we should also note that the diathermal consequence of mixing is that summertime warming of *IG* water parcels exceeds their wintertime cooling (Fig. 6c).

655 Diahaline transformation along the upper *IC* pathway is characterised by the freshening of water parcels flowing northward across OSNAP East between February-August. Interestingly, Figure 6f-9d shows that it is this substantial freshening, rather than summertime heating, which is responsible for the negative diapycnal transformation along water parcel trajectories initiated flowing north in late spring - early summer. The largest freshening along the boundary current is associated with water parcels which flow northward in the *IC* during May-June and return southward across OSNAP East via the EGC in November-December. This is consistent with observations, which show that the largest freshwater transport of the East Greenland Coastal Current (EGCC) occurs during autumn (Le Bras et al., 2018) (Daniault et al., 2011a; Le Bras et al., 2018) following the summertime accumulation of meltwater on the shelf. Moreover, observations indicate that the strongest mixing between cold, fresh EGCC water and comparatively warmer and saltier EGC water occurs in winter (Le Bras et al., 2018), concurrent with the return of the freshest upper *IC* water parcels across OSNAP East. Notably, Figure 6f indicates that upper *IC* trajectories flowing northward across the section between September-January (returning southward between March-June) experience negligible diahaline transformation alongstream, since freshwater transport in the EGCC is weakest during spring (Le Bras et al., 2018; Lin et al., 2018). Thus, the largest seasonal diapycnal transformations along the boundary current of the Irminger Sea are dominated by surface heat loss.

670 (a) Mean seasonal cycle of transport-weighted mean potential density on SAF inflow (circular markers), RR crossing (rhombus markers) and EGC outflow (square markers) for water parcels flowing northward across OSNAP East in the upper 250 m of the *IC-RR-Irm* pathway. Note that the transport-weighted mean potential densities on crossing the RR and returning to OSNAP East via the EGC are plotted at the month when water parcels originally flowed northward across OSNAP East. (b) Example water parcel trajectories illustrating the upper *IC-RR-Irm* circulation pathway within the eastern SPG. (c, d) Mean seasonal cycles of transport-weighted mean net change in potential density,  $\Delta\sigma$ , and contributions from diathermal ( $\Delta\theta$ , black

675

solid line) and diahaline ( $\Delta S$ , black dotted line) components divided into two successive diapycnal transformations in the Iceland (e, Ic-RR) and Irminger Basins (d, RR-Irm)

680 Since water flowing northward in the upper IC is sourced from relatively warm and saline SPMWs advected along the northern branch of the NAC (McCartney and Talley, 1982; Brambilla and Talley, 2008; Danialt et al., 2016), it is interesting to We next compare and contrast the character of seasonal water mass transformation along the upper IC pathway with the dominant Ic-RR-Irm overturning pathway within the eastern SPG. Figure 7 presents the seasonal density changes and their associated diathermal and diahaline components for water parcels crossing the OSNAP East section in the boundary and interior modes of seasonal watermass transformation with that of the dominant time-mean Lagrangian overturning pathway sourced from the central branch of the NAC. Figures 9a-b show that water parcels sourced from the upper 250 m and following the of the Ic-RR-Irm Ic-Irm pathway (orange box) experience net densification irrespective of the time of year that they flow northward across OSNAP East. Given that the Ic-RR-Irm Ic-Irm pathway flows from the Sub-Arctic Front to the EGC via the Reykjanes Ridge, we choose to decompose the net diapycnal transformation north of OSNAP East into two successive transformations taking place in the Iceland and Irminger Basins basins (Fig. 7e-d). Figure 7a shows that upper 9e-f). We find that upper Ic-RR-Irm Ic-Irm water parcels experience sufficient net diapycnal transformation north of OSNAP East to be transferred into the lower limb of the LMOC, irrespective of their water mass properties on inflow. ~~This is because water parcels typically recirculate on interannual timescales ( $\bar{\tau} = 1.1$  years) and are therefore guaranteed to experience at least one winter within the eastern SPG (see Fig. A1d).~~ For the lightest water parcels flowing northward in autumn, this diapycnal transformation is dominated by intense wintertime heat loss ~~manifests as a large diathermal transformation~~ (equivalent to  $\sim 0.5 \text{ kg m}^{-3}$ ) during their initial 6.8 months spent within the Iceland Basin (Fig. 7e9e). In contrast, the densest water parcels arriving at OSNAP East in spring experience wintertime diathermal transformation (equivalent to  $\sim 0.5 \text{ kg m}^{-3}$ ) during their 695 final 6.5 months spent in the Irminger Basin basin (Fig. 7d9f). Thus, we find that wintertime surface buoyancy loss ~~removes all seasonal thermohaline variability flowing northwards into the eastern SPG~~ acts as an important damping mechanism of seasonal thermohaline anomalies advected northward into the eSPG. Meanwhile, the transit times of upper Ic-RR-Irm Ic-Irm water parcels through the Iceland and Irminger Basins basins account for the 7-month phase shift in the seasonal eye-in 700 density as it decays downstream (Fig. 7a). cycles of diapycnal transformation shown in Figures 9e-f.

In addition to surface-forced diapycnal transformations, the The remarkably consistent density of the upper Ic-RR-Irm Ic-Irm pathway on returning southward across OSNAP East in the EGC ( $27.55 \pm 0.01 \text{ kg m}^{-3}$ ; Fig. A1d) additionally underscores the importance of interior mixing along water parcel trajectories. This is because interior mixing is associated with the convergence of water parcels masses in T-S space, whereas transformation by surface buoyancy fluxes leads to diverging water mass properties (Groeskamp et al., 2014; Mackay et al., 2020). The strong density compensation between year-round cooling and freshening along the upper Ic-RR-Irm Ic-Irm pathway in the Irminger Sea (Figure 7d9f) is indicative of a constant background mixing with  fresher Arctic origin waters transported in the EGCC colder and fresher waters sourced from north of the Greenland-Scotland Ridge. A closer examination shows that this mixing (freshening) along water parcel trajectories is concentrated near between Denmark Strait and the Kangerdlugssuaq Trough in the northern Irminger Basin, where observations basin. 705 On the one hand, this localised freshening of the boundary current is consistent with observations, which have found substantial 710

freshwater transports directed offshore from the East Greenland Shelf (Sutherland and Pickart, 2008; Sutherland et al., 2009; Foukal et al., 2020). ~~We therefore propose that mixing between Arctic and Atlantic water masses along the western boundary of the Irminger Sea plays an integral role in maintaining~~ However, such cooling and freshening are also consistent with the excessive turbulent mixing between the dense overflows and overlying ambient Atlantic waters documented previously in the ORCA025-GJM189 hindcast (MacGilchrist et al., 2020; Tooth et al., 2023). It therefore remains an outstanding question to what extent the stable composition of the lower limb ~~on seasonal timescales found in this simulation~~ (see Fig. 36b where  $\sigma_{LMOC} = 27.51 \pm 0.02 \text{ kg m}^{-3}$ ) :-

~~In summary, we have identified two dominant modes of seasonal Lagrangian overturning variability taking place in the upper 250 m of the eastern SPG. Approximately half of the seasonal cycle of Lagrangian overturning at OSNAP East originates from the boundary current encircling the Irminger Sea, while the remainder is sourced equally from water parcels recirculating in the interior of the Irminger and Central Iceland Basins. Seasonal diapycnal transformation along both the boundary and interior pathways is dominated by the diathermal component resulting from air-sea interaction north of OSNAP East. Although diahaline transformations are of secondary importance to boundary and interior densification, they highlight the important and contrasting roles of lateral mixing between water masses along stream. In the upper Irminger Gyre, ~~represents an artifact~~ of well-established model biases or rather underscores the importance of mixing between Atlantic, Arctic and overflow water masses along the northwestern boundary of the year-round salinification of water parcels owing to boundary-interior exchange acts to reinforce their wintertime densification. Meanwhile, water parcels flowing northward across OSNAP East in the boundary current in spring exhibit substantial freshening along stream due to enhanced mixing with Arctic-origin waters in the EGCC during the ensuing autumn. The additional 2.4 months required for water parcels to be advected along the Irminger Current also reduces the variability of water mass properties on southward outflow compared with those rapidly recirculating in the Irminger Gyre. When advective timescales are increased further, as found along our dominant overturning pathway (*Ic-RR-Irm*), intense wintertime heat loss north of OSNAP East acts to damp the seasonality of water mass properties on northward inflow, thus forming lower limb water of remarkably consistent density. Irminger Sea, as highlighted in Evans et al. (2022)~~

~~Mean Eulerian volume transport in the upper limb (i.e. above  $\sigma_{MOC}$ ) of the MOC accumulated with distance eastward along OSNAP East. The net upper limb volume transport (a) is decomposed into its respective northward (b) and southward components (c). The model bathymetry along the OSNAP East array is presented in (d). Vertical lines partition the volume transport across the section into five geographical regions corresponding to the major currents intercepted by the array: East Greenland Current (EGC), Irminger Gyre and Irminger Current (IG & IC), East Reykjanes Ridge Current (ERRC), the Central Iceland Basin and Sub-Arctic Front (CIB & SAF), and the Rockall Plateau and Rockall Trough (RP & RT).~~

## 5 Mechanisms of seasonal Eulerian overturning variability

~~We conclude our analysis by-~~

## 5 Discussion and conclusions

In this study, we investigate the nature of seasonal overturning variability within the eastern North Atlantic subpolar gyre using Lagrangian water parcel trajectories to east new light on the mechanisms responsible for seasonal Eulerian overturning variability. We begin by decomposing the net volume flux in evaluated within an eddy-permitting ocean sea-ice hindcast simulation. To complement the traditional Eulerian overturning streamfunction, we employ the recently introduced Lagrangian Overturning Function (LOF) in density-space (Tooth et al., 2023) to diagnose the net diapycnal transformation along water parcel trajectories evaluated from the northward inflows across a model-defined OSNAP East section. Our analysis demonstrates that the MOC upper limb, determined directly from the simulated velocity and potential density fields along OSNAP East, into its constituent northward and southward components during April and October, corresponding to the extrema of the MOC seasonal cycle in Figure 2b. Figure 8 indicates that, in spite of the year-round net northward transport in the upper limb, the seasonal cycle of the MOC results from changes in the southward transport above  $\sigma_{MOC}$  advective timescales over which water masses circulate within the eSPG plays a crucial role in shaping the simulated Eulerian and Lagrangian seasonal overturning variability at OSNAP East. This is highlighted in Figure 8c, which shows that the total southward

From an Eulerian perspective, we show that the net transport in the upper limb increases significantly from  $-8.7$  Sv in April, when the Eulerian overturning reaches its seasonal maximum ( $18.5$  Sv), to  $-14.4$  Sv when the MOC seasonal minimum ( $14.4$  Sv) occurs in October.

Mean Eulerian net volume transport (Sv) in the upper limb of the MOC (i.e., above  $\sigma_{MOC}$ ) for the major currents along the OSNAP East array during April and October. The major currents are defined geographically as follows: East Greenland Current (EGC,  $0 \text{ km} < x \leq 250 \text{ km}$ ), Irminger Gyre and Irminger Current (IG & IC,  $250 \text{ km} < x \leq 750 \text{ km}$ ), East Reykjanes Ridge Current (ERRC,  $750 \text{ km} < x \leq 1000 \text{ km}$ ), Central Iceland Basin and Sub-Arctic Front (CIB & SAF,  $1000 \text{ km} < x \leq 1450 \text{ km}$ ), and Rockall Plateau and Rockall Trough (RP & RT,  $1450 \text{ km} < x \leq 2300 \text{ km}$ ). Note  $x$  corresponds to the distance from Cape Farewell on the east Greenland coast. **EGC IG & IC ERRC CIB & SAF RT & RP Total Net Upper Limb Volume Transport (Sv)** April  $-2.1$   $2.4$   $-2.5$   $14.2$   $6.5$   $18.5$  October  $-4.9$   $4.2$   $-4.2$   $13.9$   $5.4$   $14.4$

Further decomposition of the seasonal upper limb transport according to the major currents crossing the OSNAP East array (Table 1) indicates that the seasonal minimum of the MOC results from the combination of a  $2.8$  Sv strengthening of the EGC southward transport above  $\sigma_{MOC}$  and a  $1.1$  Sv weakening of the southern NAC branch feeding the Rockall Trough and Plateau. This agrees with the recent results of Wang et al. (2021), who demonstrated that variations in the southward transport along the western boundary of the Irminger Sea play a prominent role in modulating the of the MOC exhibits a pronounced seasonal cycle of overturning  $4.1$  Sv at OSNAP East, consistent with estimates made using both observations and ocean reanalyses (Mercier et al., 2015; Wang et al., 2021). Moreover, Wang et al. (2021) showed that the seasonality of the EGC upper limb transport is principally explained by seasonal density changes in the upper Irminger Sea projecting onto the mean barotropic transport of the western boundary current. To explore this further, Figure 9 presents the mean potential density field along OSNAP East in April (MOC maximum) and October (MOC minimum) and the corresponding location of  $\sigma_{MOC}$ . In April, we find that the erosion of stratification, owing to intense wintertime heat loss, permits deep convective mixing in

the Irminger Sea interior (de Jong et al., 2012; de Jong and de Steur, 2016; Piron et al., 2016), such that  $\sigma_{MOC}$  ( $27.57 \text{ kg m}^{-3}$  in April) outcrops at the surface (Fig. 9a). As a consequence, the total northward transport above  $\sigma_{MOC}$  along OSNAP East is reduced, since a substantial fraction of the water flowing northward in the Irminger Sea does so in the lower seasonality in the strength of Eulerian overturning is closely related to the density structure along the Irminger Sea western boundary. The weakest Eulerian overturning occurs in October when the outflowing EGC is lightest, yielding a large southward transport ( $-4.9 \text{ Sv}$ ) in the upper limb of the MOC (de Jong et al., 2020). Along the western boundary, the isopycnal of maximum overturning slopes steeply with distance offshore during spring, resulting in a weak upper limb transport in the EGC ( $-2.1 \text{ Sv}$ , Table 1). Thus, since less southward transport is available to compensate for the stronger northward transport above  $\sigma_{MOC}$  in the NAC (20.7 Sv, Table 1), the MOC reaches a seasonal maximum. A contrasting picture emerges in October, when Figure 9b shows that surface heating through summer has restored the stratification in the upper Irminger Sea. This is in agreement with the recent observations of de Jong et al. (2020), who found the lowest monthly mean density along OSNAP East during October. Since the depth of  $\sigma_{MOC}$  in Figure 9b exceeds 100 m throughout the entire Irminger Basin, there is hence a larger northward upper limb. We find the largest Eulerian overturning in April when the density structure of the EGC, closely reflecting that of the basin interior, results in the weakest southward transport ( $-2.1 \text{ Sv}$ ) within the density classes of the upper limb and the strongest southward transport in the Irminger Gyre and the Irminger Current ( $4.2 \text{ Sv}$ ). However, this is more than compensated for by the vertical migration of the isopycnal of maximum overturning offshore of the East Greenland shelfbreak, which enables water flowing southward in the upper 200 m of the EGC to be included within the lighter MOC upper limb ( $\sigma_{MOC} = 27.50 \text{ kg m}^{-3}$  in October) as recently observed by Le Bras et al. (2020). This, in lower limb. This agrees closely with the results of Holte and Straneo (2017), who used Argo profiling floats to show that the MOC seasonal cycle in the Labrador Sea peaks in spring in conjunction with the weaker transport of warm, saline water flowing northward in the NAC (a change of  $-1.4 \text{ Sv}$ ), is therefore responsible for the MOC seasonal minimum in October outflow of newly formed LSW in the Labrador Current.

Mean potential density along OSNAP East in (a) April and (b) October overlaid by the corresponding mean isopycnal of maximum Eulerian overturning (April:  $\sigma_{MOC} = 27.57 \text{ kg m}^{-3}$ , October:  $\sigma_{MOC} = 27.50 \text{ kg m}^{-3}$ ), denoting the seasonal interface between the upper and lower limbs of the MOC.

In contrast with previous studies which attribute the seasonality of Eulerian overturning to the seasonal export of western boundary density anomalies alone (Brandt et al., 2007; Holte and Straneo, 2017; Wang et al., 2021), we also highlight the important role of seasonal wind stress forcing over the Irminger basin. In addition to the deepening of  $\sigma_{MOC}$  along the conclusion of Wang et al. (2021), we do not find that the seasonal cycle of the MOC can be accounted for by changes in the density structure of the western Irminger Basin alone. Rather, we propose that variations in the velocity field of the EGC act in conjunction with seasonal migrations of  $\sigma_{MOC}$  to drive the seasonality of Eulerian overturning at OSNAP East. To demonstrate this, we return to the water parcels recirculating exclusively within the upper 250 m of the Irminger Basin (upper *Irm-Irm*), where we find a strong seasonal signal in the median amount of time water parcels spend north of OSNAP East (Fig. ??). Figure ??a shows that recirculation times along both the western boundary of the Irminger Sea, the enhanced upper limb EGC transport responsible for the MOC minimum in October is owed to a convergence of water parcels which flowed northward across OSNAP East in the upper *IC* and *IG* pathways are longest when water parcels flow northward across OSNAP East during

winter and are shortest when they cross the section during summer. For the upper *IC* pathway, this amounts to water parcels typically spending 8 months circulating along the boundary current following initialisation in February compared with only 6 months when initialised in August. While this gives us a useful indication of the seasonality in the large-scale circulation north of OSNAP East, it is the transition in upper *Irm-Irm* recirculation times through spring (Fig. ??a) which is the crucial driver of seasonal MOC variability. This is because the decrease in the recirculation times of water parcels crossing OSNAP East northwards in the upper *IC* between February-May produces a convergence of water parcels flowing southward in the EGC during autumn. The strongest convergence occurs in October, consistent with the observed intensification of the upper EGC at OSNAP East during autumn (Le Bras et al., 2018; Pacini et al., 2020), and amounts to a 1.0 Sv negative anomaly in the full-depth transport of the EGC. While the magnitude of this transport anomaly remains small compared with the typical magnitude of the EGC in this simulation (31.0 Sv), its surface-intensified nature has important consequences for the strength of the MOC at OSNAP East. Figure ??a shows that the convergence of upper *Irm-Irm* water parcels within the EGC occurs almost exclusively within the upper limb of the MOC. Thus, by acting in concert with the deepening of  $\sigma_{MOC}$  during late summer and autumn (Fig. 9b), the convergence of upper *Irm-Irm* water parcels within the boundary current can explain 2.6 Sv of the 2.8 Sv increase in the upper limb EGC southward transport between April and October, accounting for almost two-thirds of the amplitude of the MOC seasonal cycle at OSNAP East (4.2 Sv).

Previous studies have highlighted the close relationship between seasonal variations in the large-scale circulation 250 m of the Irminger Sea and wind stress forcing acting over the basin (Le Bras et al., 2018). To determine whether local wind stress forcing can account for the seasonality of basin during spring. This convergence is the result of decreasing water parcel recirculation times in the upper Irminger Sea, we next compare the character of upper *IC* trajectories flowing northward across OSNAP East in February and August, corresponding to which is consistent with a spin-up of the eSPG in response to increasing wind stress curl acting over the basin during the ensuing autumn-winter (Daniault et al., 2011a; Le Bras et al., 2018; Pacini et al., 2020). We therefore propose that the seasonal cycle of Eulerian overturning at OSNAP East arises from a complex combination of seasonal dense water formation along the western boundary of the longest and shortest recirculation times, respectively. Figure ??b shows that the longer median recirculation times of upper *IC* water parcels flowing northward across OSNAP East in February is due to their slower advection along the boundary current through spring-summer. The weakening of the boundary current is explained by the springtime spin-down of the SPG circulation owing to the decrease in wind stress curl acting over the Irminger Sea (?). In addition to their slower recirculation times along the boundary current, water parcels flowing northward in February are more likely to be entrained into slower circulation pathways in the basin interior, resulting in a longer tail in the distribution of recirculation times in Figure ??c. The shorter recirculation times exhibited by upper *IC* water parcels flowing northward in August results from the autumn-wintertime spin-up of the SPG during their recirculation north of OSNAP East. Figure ??b shows that water parcels flowing northward in August experience especially fast advection within the EGC, where the strongest north-easterly winds act along-stream. This is consistent with the study of Le Bras et al. (2018), who found that seasonal variations in the wind stress curl, and by extension the EGC transport, are largely determined by changes in the local wind stress field acting along the East Greenland coast.



(a) Seasonal cycle of median recirculation times north of OSNAP East for water parcels initialised in the upper 250 m of the Irminger Current (*IC*, purple) and Irminger Gyre (*IG*, pink) pathways. The total volume transport of upper *Irm-Irm* water parcels flowing southward in the EGC within the upper limb (i.e., above  $\sigma_{MOC}$ ) is given by the solid black line ( $V_{EGC}$ ). Note that water parcel volume transports are plotted according to the month during which they cross OSNAP East southward in the EGC. (b) Example water parcel trajectories flowing northward in the upper 250m of the Irminger Current during February (pink) and August (green) 2000. The associated median recirculation times are also coloured accordingly in a). Way point markers show the locations of water parcels remaining within the boundary current at 60- (circles) and 120-days (squares) following initialisation. Trajectories are superimposed on filled contours of the difference between the mean winter (DJF) and summer (JJA) northward component of the wind stress fields calculated between 1976-2015. The time-mean wind stress field (1976-2015) is shown by the overlying vectors included at the centre of every 4<sup>th</sup> model grid cell. (c) Distributions of upper *IC* recirculation times determined from all of the water parcels flowing northward across OSNAP East during February (pink) and August (green) between 1976-2008 (i.e., 33 initialisations for each month).

In this study, we investigate the nature of seasonal overturning variability within the eastern North Atlantic SPG using Lagrangian water parcel trajectories evaluated within an eddy-permitting ocean sea-ice hindcast simulation. We employ the recently introduced Lagrangian Overturning Function (LOF) in density-space, complementing the traditional Eulerian overturning streamfunction, to diagnose the net diapycnal transformation integrated along water parcel trajectories traced from the northward inflows across a model-defined OSNAP East section. By decomposing the LOF according to the individual circulation pathways of the eastern SPG, we determine the principal routes by which the seasonal signal of water mass transformation north of OSNAP East can imprint onto the strength of overturning recorded at the section. Furthermore, our analysis highlights the crucial role of water parcel recirculation times within the eastern SPG in driving both Lagrangian and Eulerian overturning variability on seasonal timescales. Irminger Sea and the wind-driven modulation of water parcel recirculation times, which determines how efficiently density anomalies can be exported downstream. As such, the proximity of the OSNAP East array to regions of dense water formation exercises an important influence on the seasonality of Eulerian overturning measured at the section. For example, the amplitude of seasonal MOC variability would likely be reduced if the OSNAP East array were deployed further south, since a smaller fraction of lower limb waters would be exported across the section within a year of their formation (Le Bras et al., 2020).

From a Lagrangian perspective, we show that the formation of upper NADW along the cyclonic pathways of the eastern SPG eSPG is strongly dependent upon when the time of year water parcels flow northwards northward across OSNAP East. The lightest water parcels, flowing northward during autumn, undergo arriving at the section in autumn, experience the greatest positive diapycnal transformation due to intense wintertime surface buoyancy heat loss along-stream and constitute the largest strongest seasonal volume flux into the lower limb. Meanwhile, the weakest volume flux into the lower limb is associated with the densest water parcels arriving at OSNAP East in spring and results from negative diapycnal transformation owing to summertime surface buoyancy gain summertime heating along-stream. The pronounced seasonal cycle of Lagrangian overturning within the eastern SPG is therefore predicated upon water parcels preserving the seasonal signature of surface forced water mass transformation north of OSNAP East. The magnitude of seasonal variability ( $SD = \pm 2.2$



Sv) remains small compared with the time-mean Lagrangian overturning (8.9 Sv), however, since only water parcels which spend less than 8.5 months north of OSNAP East are able to avoid irreversible diapycnal transformation into the lower limb. The majority of northward transport in the upper limb of the LMOC, sourced from the central and southern NAC branches, exceeds this threshold timescale, crossing the Reykjanes Ridge directly north of OSNAP East in order to reach the EGC within 1-3 years. Pathways crossing the Reykjanes Ridge therefore dominate the mean strength of the Lagrangian overturning since water parcels are almost guaranteed to form upper NADW along stream because they experience at least one winter of intense surface buoyancy loss north of OSNAP East. In contrast, seasonal Lagrangian overturning variability originates from the northward inflows into the Irminger and Central Iceland Basins, where the shorter path around the cyclonic SPG ( $\leq 8.5$  months) enables some water parcels to undergo summertime buoyancy gain and avoid re-densification during the ensuing autumn-winter. The location of the OSNAP East array therefore has a significant influence on the seasonality of the measured Lagrangian overturning, by determining the advective timescales on which water parcels recirculate north of the section. For example, deploying the OSNAP East array further south would likely reduce the amplitude of seasonal Lagrangian overturning variability, given that a greater proportion of recirculating water parcels would experience at least one winter north of the section and hence be transferred into the lower limb.

Given the asymmetry between stronger wintertime surface buoyancy loss and weaker summertime buoyancy gain over the Iceland and Irminger Basins (de Boisséson et al., 2010; Brambilla et al., 2008; Xu et al., 2018b), it is also interesting to frame seasonal Lagrangian overturning variability somewhat analogously to "Stommel's Demon" (Stommel, 1979; Williams et al., 1995). That is to say, water parcels advected northwards northward across OSNAP East in the upper limb of the LMOC are participating in a recirculation race against time to avoid wintertime diapycnal transformation into the lower limb. The majority of water parcels upper limb water parcels, sourced from the central and southern NAC branches, are unsuccessful and hence contribute to determine the mean strength of Lagrangian overturning within the eastern SPG. However, a small collection of water parcels at a specific time of year recirculate sufficiently quickly to imprint onto the seasonality of Lagrangian overturning downstream. eSPG. In contrast, the seasonal cycle of Lagrangian overturning originates from rapidly recirculating ( $\leq 8.5$  months) water parcels in the upper Irminger and Central Iceland basins, whose along-stream diapycnal transformation is dependent on their time of arrival at OSNAP East.

The recent study of MacGilchrist et al. (2021) extended the concept of a seasonal "Demon" by demonstrating that the subduction of water parcels into the interior of the SPNA is additionally modulated by interannual variations in atmospheric forcing, such as the North Atlantic Oscillation (NAO; Hurrell 1995). While-Although it is beyond the scope of this study, it would be interesting to establish whether the seasonal cycle of Lagrangian overturning exhibits a similar sensitivity to interannual variations in surface buoyancy forcing over the Iceland and Irminger Basinsbasins. It may alternatively be the case that enhanced surface heat loss, such as that associated with the strong positive phase strong positive phases of the NAO during the early-1990s (Visbeck et al., 2003; Bersch et al., 2007), would be of secondary importance to changes in water parcel recirculation times owing to the concordant intensification and contraction of the SPG subpolar gyre circulation (Curry and McCartney, 2001; Flatau et al., 2003; Pollard et al., 2004). Thus, we might anticipate an increase in the amplitude of seasonal Lagrangian overturning variability following positive phases of the NAO since the westward retreat of the Subarctic Front

(Pollard et al., 2004; Bersch et al., 1999) favours greater inflow to the Irminger and Central Iceland basins, which dominate the seasonality of Lagrangian overturning at OSNAP East.

Through a detailed investigation of the circulation pathways responsible for the seasonal cycle of Lagrangian overturning at OSNAP East, we show that 75% of all overturning seasonality originates from identify two dominant modes of seasonal Lagrangian overturning variability operating in the upper 250 m of the Irminger Sea. The remaining seasonality eSPG. Approximately half of the seasonal cycle of Lagrangian overturning at OSNAP East is sourced from the interior recirculation in the upper 250 m of Central Iceland Basin. We identify two dominant modes of seasonal overturning variability according to whether a water parcel circulates along the longer path encircling the boundary of the water parcels rapidly recirculating in the interior of the Central Iceland and Irminger basins ( $\bar{\tau} \approx 4$  months), while the remainder originates from the longer boundary current encircling the Irminger Sea ( $\bar{\tau} \approx 6$  months) or follows a faster route ( $\bar{\tau} \approx 4$  months) within the interior of the Irminger and Central Iceland Basins. Although, Although seasonal diapycnal transformation along both boundary and interior pathways is dominated by the surface-forced diathermal transformation dominates the along-stream densification of both modes diathermal component, diahaline transformations still play an important role in shaping the character of seasonal overturning variability. Water parcels rapidly recirculating within the Irminger Gyre become lighter (denser) when flowing northward across OSNAP East between February–July (August–Jan) as a result of surface heat gain (loss), which is weakly compensated by highlight the important and contrasting roles of lateral mixing between water masses along-stream. In the upper Irminger Gyre, the year-round salinification owing to lateral mixing with warmer and saltier SPMWs advected along the boundary current. Conversely of water parcels owing to boundary-interior exchange acts to reinforce their wintertime densification. Meanwhile, water parcels advected along the longer the Irminger Current pathway only become lighter when flowing northward across OSNAP East in May and June. This narrow window of negative diapycnal transformation is principally explained by the enhanced freshening of water parcels downstream in the EG the Irminger Current during spring experience substantial freshening downstream, consistent with the greater mixing observed between boundary current and Arctic-origin waters along the shelfbreak during winter (Le Bras et al., 2018). Our proposition that the contrasting diahaline changes along the boundary current (freshening) and within the basin interior (salinification) result from mixing is supported by Xu et al. (2018a), who found that, on average, the mixing-induced diapycnal transformation is negative (lightening) on the inshore side of the boundary current and positive (densification) between the boundary current and the interior. Interestingly, for water parcels flowing northward in the upper 250 m of the Irminger Current in winter, we find negligible diahaline transformation along-stream, indicating that densification is entirely due to surface heat loss along the boundary current. This aligns with previous studies, which have documented the seasonal evolution of boundary currents properties in terms of wintertime diapycnal transformation due to air-sea interaction and summertime along-isopycnal mixing owing to boundary-interior exchange within the SPNA (Cuny et al., 2002; Huang et al., 2021). While we have only sought to infer the contributions of air-sea interaction and mixing to the net densification along water parcel trajectories in this study, it would prove valuable for a future study to formally diagnose their respective contributions to the diathermal and diahaline transformations governing the densification of water masses within the SPGeSPG.

950 ~~Our Lagrangian analysis~~ The Lagrangian analysis presented in this study also demonstrates how the longest circulation pathways within the ~~eastern SPG~~ eSPG maintain the consistent water mass properties of the LMOC lower limb flowing southward across OSNAP East. By ~~examining seasonal water mass transformations~~ decomposing the seasonal cycle of diapycnal transformation along the dominant ~~Ic-RR-Irm~~ Ic-Irm overturning pathway, we show that, provided water parcels spend at least one winter north of OSNAP East, they will ~~undergo~~ experience sufficient surface-forced diathermal transformation to form 955 upper ~~ISIW~~ NADW, irrespective of their properties on inflow. We therefore ~~propose~~ suggest that wintertime surface buoyancy loss over the Iceland and Irminger ~~Basins acts as a crucial~~ basins constitutes an important damping mechanism for seasonal thermohaline variability imported ~~from the NAC upstream~~ northward across OSNAP East. Meanwhile, the stable year-round composition of lower limb waters flowing southward in the EGC results from ~~mixing with~~ a constant background mixing with both overflow and Arctic-origin waters along the ~~western-northwestern~~ boundary of the Irminger ~~Basin~~ Sea. Interestingly, ~~the~~ 960 ~~recent~~ our findings may also be relevant to the recent observational study of Fu et al. (2020), ~~which~~ shows that the ~~insensitivity of subpolar overturning to large-scale thermohaline variability~~ strength of the subpolar MOC has remained remarkably stable during the last three decades, in spite of the profound hydrographic changes recorded in the upper 1000 m of the eSPG (e.g. Holliday et al. 2008; Lozier et al. 2008; Thierry et al. 2008; Holliday et al. 2020; Desbruyères et al. 2021) ~~may also occur on decadal timescales in the eastern SPG. This implies~~. This is because we have shown that, given a sufficiently long ~~advective~~ 965 ~~timescale within the eastern SPG~~ recirculation time within the eSPG, the combination of surface buoyancy loss and interior mixing north of OSNAP East can act as a sink of upper-ocean thermohaline variability and ~~therefore maintain the stability of the MOC~~.

From an Eulerian perspective, we show that the net transport in the upper limb of the MOC exhibits a pronounced seasonal cycle of 4.1 Sv at OSNAP East, ~~consistent with estimates made using both observations and ocean reanalyses within the~~ 970 ~~eastern SPG (Mercier et al., 2015; Wang et al., 2021). Moreover, seasonality in the strength of Eulerian overturning is closely related to the density structure along the Irminger Sea western boundary. The weakest Eulerian overturning occurs in October when the outflowing EGC is lightest, yielding a large southward transport (-4.9 Sv) in the upper limb of the MOC. We find the largest Eulerian overturning in April when the density structure of the EGC, closely reflecting that of the basin interior, results in the weakest southward transport (-2.1 Sv) within the density classes of the upper limb and the strongest southward transport in the~~ thereby maintain a consistent volume flux in the lower limb. ~~This agrees closely with the results of Holte and Straneo (2017), who used Argo profiling floats to show that the MOC seasonal cycle in the Labrador Sea peaks in spring in conjunction with the outflow of newly formed LSW in the Labrador Current. However, in contrast with previous studies which attribute the seasonality of overturning to the seasonal export of western boundary density anomalies alone (Brandt et al., 2007; Holte and Straneo, 2017; Wang et al., 2021), we also highlight the important role of seasonal water parcel~~ 975 ~~recirculation times in the upper Irminger Sea. In addition to the deepening of  $\sigma_{MOC}$  along the western boundary of the Irminger Sea, the enhanced upper limb EGC transport responsible for the MOC minimum in October is owed to a convergence of~~ Irm-Irm water parcels which flowed northward across OSNAP East in the upper 250 m of the Irminger Basin through spring. ~~This convergence is the result of decreasing recirculation times of upper~~ Irm-Irm water parcels north of OSNAP East,

which we propose is consistent with a spin-up of the SPG in response to the intensification of basin-scale wind stress forcing during the ensuing autumn-winter (Le Bras et al., 2018; Pacini et al., 2020).

This study demonstrates that the advective timescales over which water masses circulate within the eastern SPG plays a critical role in shaping the simulated Eulerian and Lagrangian seasonal overturning variability at OSNAP East. However, what remains unclear is how our principal findings might change in an ocean sea-ice hindcast simulation performed at eddy-rich rather than eddy-permitting resolution (e.g., Böning et al. 2016; Marzocchi et al. 2015; Biastoch et al. 2021; Hirschi et al. 2020). On the one hand, we might anticipate that advective timescales will increase with horizontal resolutions since improved and thus several limitations should be acknowledged. Firstly, the water parcel recirculation timescales identified within the eSPG will be sensitive to our choice of model horizontal resolution, since this governs the representation of submesoscale and mesoscale dynamics produces more dispersive water parcel trajectories (Gary et al., 2011). However, in particular, the study of Blanke et al. (2012) shows that the inclusion of small-scale structures in high resolution velocity fields finer-scale structures in the velocity fields simulated by eddy-rich models reduces water parcel transit times despite also increasing the complexity of trajectories (Gary et al., 2011). This is further compounded by the stronger SPG-subpolar gyre circulation simulated in eddy-rich models compared with those configured at eddy-permitting resolution (Jackson et al., 2020; Hirschi et al., 2020), which favours shorter advective timescales and recirculation times and hence a larger seasonal overturning signal in the eastern SPNA. Lagrangian overturning signal at OSNAP East.

Secondly, the mixing-induced diapycnal transformations along water parcel trajectories will be dependent upon both model resolution and the chosen parameterisations of lateral eddy mixing and turbulent entrainment in the bottom boundary layer. Although not included in this ORCA025 configuration, previous studies have shown that implementing a modified form of the mesoscale eddy mixing scheme of Gent and McWilliams (1990) at eddy-permitting resolution can significantly improve model hydrography in the SPNA by reducing spurious diapycnal mixing between boundary and interior water masses (Deacu and Myers, 2005a, b). Given their ability to explicitly resolve the effects of mesoscale eddies, we would also expect eddy-rich models (e.g., Böning et al. 2016; Marzocchi et al. 2015; Biastoch et al. 2021; Hirschi et al. 2020) to simulate more realistic mixing along water parcel trajectories. However, this is partly undermined by the well-documented warming and salinification trends in the Labrador and Irminger Seas at eddy-rich resolution (Treguier et al., 2005; Xu et al., 2013; Marzocchi et al., 2015; Pennelly and Myers, 2020), which yield significantly larger than observed diapycnal transformation and hence overturning within the SPNA (Hirschi et al., 2020). Establishing whether the mechanisms governing overturning seasonality are consistent across numerical models should therefore be considered an ongoing priority, especially given that the accurate assessment of long-term trends in the strength of the subpolar MOC is predicated on adequately resolving the variability simulated on seasonal-seasonal-interannual timescales.

*Code and data availability.* The Lagrangian trajectories used in the analysis can be obtained from <https://doi.org/10.5281/zenodo.6573900>.

The Lagrangian trajectory code TRACMASS, developed by Aldama-Campino et al. (2020), is available from <https://doi.org/10.5281/zenodo.4337926>.

Full details of the NEMO ocean model configuration, including access to forcing files, is available on GitHub (<https://github.com/meom-configurations/ORCA025.L75-GJM189.git>), and has been released with an associated DOI (<https://doi.org/10.5281/zenodo.4626012>.)

*Author contributions.* OJT, HLJ and CW defined the overall research problem and methodology. OJT conducted the Lagrangian experiments, performed the analyses and wrote the manuscript. All authors (OJT, HLJ, CW, DGE) discussed and refined the text and contributed to the interpretation of results.

1020

*Competing interests.* The authors declare that the research was conducted in the absence of any conflicts of interest.

*Acknowledgements.* OJT is grateful for the financial support of the UK Natural Environment Research Council (NE/S007474/1). HLJ was supported by the NERC-NSF grant SNAP-DRAGON (NE/T013494/1). CW was jointly supported by the NERC LTS-S CLASS (Climate-Linked Atlantic Sector Science) grant (NE/R015953/1) and the NERC LTS-M CANARI (Climate change in the Arctic-North Atlantic Region and Impacts on the UK) grant (NE/W004984/1). DGE was supported by the NERC LTS-S CLASS grant (NE/R015953/1). We would like to thank the European Drakkar project, who carried out the hindcast simulation, and ~~to~~ J. M. Molines and C. Talandier, who kindly provided the data. We additionally thank Laura Jackson, who kindly provided the code to extract the coordinates of OSNAP East array from the ORCA025 model grid.

1025

## Appendix A

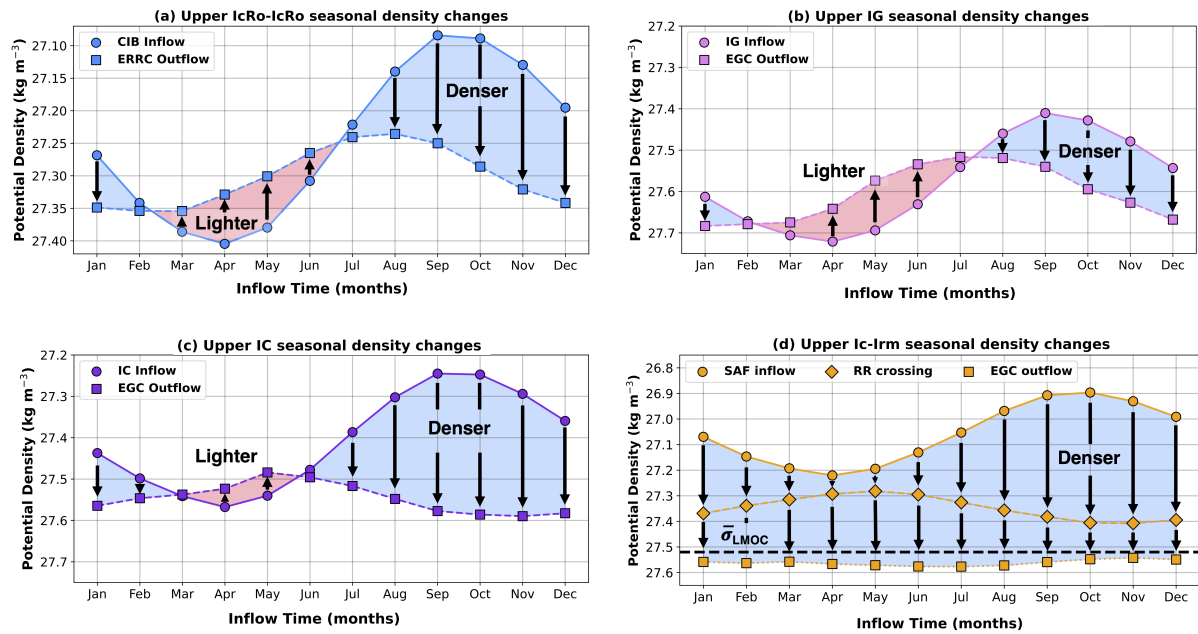


**Figure A1.** Mean seasonal cycles of the transport-weighted mean potential density on northward inflow and southward outflow crossings of the OSNAP East section for the upper 250 m of the (a) *IcRo-IcRo*, (b) *IG*, (c) *IC* pathways. (d) Same as (a-c) for Sub-Arctic Front inflow (circular markers), Reykjanes Ridge crossing (rhombus markers) and East Greenland Current outflow (square markers) for the upper 250 m of the *Ic-Irm* pathway. Note that transport-weighted mean potential densities on southward outflow (a-d) and crossing the Reykjanes Ridge (d) are plotted at the month when water parcels originally flowed northward across the OSNAP East section.

1030 **References**

- Aldama-Campino, A., Döös, K., Kjellsson, J., and Jönsson, B.: TRACMASS: Formal release of version 7.0 (v7.0-beta). Zenodo., <https://doi.org/10.5281/zenodo.4337926>, 2020.
- Asbjørnsen, H., Johnson, H. L., and Arthun, M.: Variable Nordic Seas Inflow Linked to Shifts in North Atlantic Circulation, *Journal of Climate*, 34, 7057–7071, <https://doi.org/10.1175/JCLI-D-20-0917.1>, 2021.
- 1035 Barnier, B., Madec, G., Penduff, T., Molines, J. M., Treguier, A. M., Le Sommer, J., Beckmann, A., Biastoch, A., Böning, C., Dengg, J., Derval, C., Durand, E., Gulev, S., Remy, E., Talandier, C., Theetten, S., Maltrud, M., McClean, J., and De Cuevas, B.: Impact of partial steps and momentum advection schemes in a global ocean circulation model at eddy-permitting resolution, *Ocean Dynamics*, 56, 543–567, <https://doi.org/10.1007/s10236-006-0082-1>, 2006.
- Bersch, M., Meincke, J., and Sy, A.: Interannual thermohaline changes in the northern North Atlantic 1991-1996, *Deep-Sea Research Part II: Topical Studies in Oceanography*, 46, 55–75, [https://doi.org/10.1016/S0967-0645\(98\)00114-3](https://doi.org/10.1016/S0967-0645(98)00114-3), 1999.
- 1040 Bersch, M., Yashayaev, I., and Koltermann, K. P.: Recent changes of the thermohaline circulation in the subpolar North Atlantic, *Ocean Dynamics*, 57, 223–235, <https://doi.org/10.1007/s10236-007-0104-7>, 2007.
- Biastoch, A., Böning, C. W., Getzlaff, J., Molines, J.-M., and Madec, G.: Causes of Interannual–Decadal Variability in the Meridional Overturning Circulation of the Midlatitude North Atlantic Ocean, *Journal of Climate*, 21, 6599 – 6615, <https://doi.org/10.1175/2008JCLI2404.1>, 2008.
- 1045 Biastoch, A., Schwarzkopf, F. U., Getzlaff, K., Rühs, S., Martin, T., Scheinert, M., Schulzki, T., Handmann, P., Hummels, R., and Böning, C. W.: Regional imprints of changes in the Atlantic Meridional Overturning Circulation in the eddy-rich ocean model VIKING20X, *Ocean Science*, 17, 1177–1211, <https://doi.org/10.5194/os-17-1177-2021>, 2021.
- Blanke, B., Bonhommeau, S., Grima, N., and Drillet, Y.: Sensitivity of advective transfer times across the North Atlantic Ocean to the temporal and spatial resolution of model velocity data: Implication for European eel larval transport, *Dynamics of Atmospheres and Oceans*, 55-56, 22–44, <https://doi.org/https://doi.org/10.1016/j.dynatmoce.2012.04.003>, 2012.
- 1050 Böning, C. W., Behrens, E., Biastoch, A., Getzlaff, K., and Bamber, J. L.: Emerging impact of Greenland meltwater on deepwater formation in the North Atlantic Ocean, *Nature Geoscience*, 9, 523–527, <https://doi.org/10.1038/ngeo2740>, 2016.
- Brambilla, E. and Talley, L. D.: Subpolar mode water in the northeastern Atlantic: 1. Averaged properties and mean circulation, *Journal of Geophysical Research: Oceans*, 113, 1–18, <https://doi.org/10.1029/2006JC004062>, 2008.
- 1055 Brambilla, E., Talley, L. D., and Robbins, P. E.: Subpolar mode water in the northeastern Atlantic: 2. Origin and transformation, *Journal of Geophysical Research: Oceans*, 113, 1–16, <https://doi.org/10.1029/2006JC004063>, 2008.
- Brandt, P., Funk, A., Czeschel, L., Eden, C., and Böning, C. W.: Ventilation and transformation of Labrador Sea water and its rapid export in the deep Labrador Current, *Journal of Physical Oceanography*, 37, 946–961, <https://doi.org/10.1175/JPO3044.1>, 2007.
- 1060 Bringedal, C., Eldevik, T., Øystein Skagseth, Spall, M. A., and Østerhus, S.: Structure and Forcing of Observed Exchanges across the Greenland–Scotland Ridge, *Journal of Climate*, 31, 9881 – 9901, <https://doi.org/10.1175/JCLI-D-17-0889.1>, 2018.
- Bryden, H. L., Johns, W. E., King, B. A., McCarthy, G., McDonagh, E. L., Moat, B. I., and Smeed, D. A.: Reduction in Ocean Heat Transport at 26°N since 2008 Cools the Eastern Subpolar Gyre of the North Atlantic Ocean, *Journal of Climate*, 33, 1677 – 1689, <https://doi.org/10.1175/JCLI-D-19-0323.1>, 2020.
- 1065 Buckley, M. W. and Marshall, J.: Observations, inferences, and mechanisms of the Atlantic Meridional Overturning Circulation: A review, *Reviews of Geophysics*, 54, 5–63, <https://doi.org/10.1002/2015RG000493>, 2016.



- Böning, C. W., Scheinert, M., Dengg, J., Biastoch, A., and Funk, A.: Decadal variability of subpolar gyre transport and its reverberation in the North Atlantic overturning, *Geophysical Research Letters*, 33, <https://doi.org/https://doi.org/10.1029/2006GL026906>, 2006.
- 1070 Chafik, L. and Rossby, T.: Volume, Heat, and Freshwater Divergences in the Subpolar North Atlantic Suggest the Nordic Seas as Key to the State of the Meridional Overturning Circulation, *Geophysical Research Letters*, 46, 4799–4808, <https://doi.org/10.1029/2019GL082110>, 2019.
- Chafik, L., Holliday, N. P., Bacon, S., and Rossby, T.: Irminger Sea Is the Center of Action for Subpolar AMOC Variability, *Geophysical Research Letters*, 49, e2022GL099133, <https://doi.org/https://doi.org/10.1029/2022GL099133>, 2022.
- 1075 Cunningham, S. a., Kanzow, T., Rayner, D., Baringer, M. O., Johns, W. E., Marotzke, J., Longworth, H. R., Grant, E. M., Hirschi, J. J., Beal, L. M., Meinen, C. S., and Bryden, H. L.: Temporal Variability of the Atlantic Meridional Overturning Circulation at 26.5 degrees N, *Science*, 317, 935–938, <https://doi.org/10.1126/science.1141304>, 2007.
- Cuny, J., Rhines, P. B., Niiler, P. P., and Bacon, S.: Labrador Sea boundary currents and the fate of the Irminger Sea Water, *Journal of Physical Oceanography*, 32, 627–647, [https://doi.org/10.1175/1520-0485\(2002\)032<0627:LSBCAT>2.0.CO;2](https://doi.org/10.1175/1520-0485(2002)032<0627:LSBCAT>2.0.CO;2), 2002.
- 1080 Curry, R. G. and McCartney, M. S.: Ocean Gyre Circulation Changes Associated with the North Atlantic Oscillation, *Journal of Physical Oceanography*, 31, 3374–3400, [https://doi.org/10.1175/1520-0485\(2001\)031<3374:OGCCAW>2.0.CO;2](https://doi.org/10.1175/1520-0485(2001)031<3374:OGCCAW>2.0.CO;2), 2001.
- Daniault, N., Lherminier, P., and Mercier, H.: Circulation and Transport at the Southeast Tip of Greenland, *Journal of Physical Oceanography*, 41, 437 – 457, <https://doi.org/10.1175/2010JPO4428.1>, 2011a.
- Daniault, N., Lherminier, P., and Mercier, H.: The 1992–2009 transport variability of the East Greenland-Irminger Current at 60°N, *Geophysical Research Letters*, 38, L07601, <https://doi.org/10.1029/2011GL046863>, 2011b.
- 1085 Daniault, N., Mercier, H., Lherminier, P., Sarafanov, A., Falina, A., Zunino, P., Pérez, F. F., Ríos, A. F., Ferron, B., Huck, T., Thierry, V., and Gladyshev, S.: The northern North Atlantic Ocean mean circulation in the early 21st century, *Progress in Oceanography*, 146, 142–158, <https://doi.org/10.1016/j.pocean.2016.06.007>, 2016.
- de Boisséson, E., Thierry, V., Mercier, H., and Caniaux, G.: Mixed layer heat budget in the Iceland Basin from Argo, *Journal of Geophysical Research: Oceans*, 115, 1–15, <https://doi.org/10.1029/2010JC006283>, 2010.
- 1090 de Boisséson, E., Thierry, V., Mercier, H., Caniaux, G., and Desbruyères, D.: Origin, formation and variability of the Subpolar Mode Water located over the Reykjanes Ridge, *Journal of Geophysical Research: Oceans*, 117, <https://doi.org/10.1029/2011jc007519>, 2012.
- de Jong, M. F. and de Steur, L.: Strong winter cooling over the Irminger Sea in winter 2014–2015, exceptional deep convection, and the emergence of anomalously low SST, *Geophysical Research Letters*, 42, 7106–7113, <https://doi.org/10.1002/2016GL069596>, 2016.
- de Jong, M. F., Van Aken, H. M., Våge, K., and Pickart, R. S.: Convective mixing in the central Irminger Sea: 2002–2010, *Deep-Sea Research Part I: Oceanographic Research Papers*, 63, 36–51, <https://doi.org/10.1016/j.dsr.2012.01.003>, 2012.
- 1095 de Jong, M. F., de Steur, L., Fried, N., Bol, R., and Kritsotakis, S.: Year-Round Measurements of the Irminger Current: Variability of a Two-Core Current System Observed in 2014–2016, *Journal of Geophysical Research: Oceans*, 125, e2020JC016193, <https://doi.org/https://doi.org/10.1029/2020JC016193>, 2020.
- Deacu, D. and Myers, P. G.: Effect of a Variable Eddy Transfer Coefficient in an Eddy-Permitting Model of the Subpolar North Atlantic Ocean, *Journal of Physical Oceanography*, 35, 289 – 307, <https://doi.org/10.1175/JPO-2674.1>, 2005a.
- 1100 Deacu, D. and Myers, P. G.: Analysis of an 80-Year Integration of a 1/3-Degree Ocean Model of the Subpolar North Atlantic, *Journal of Oceanography*, 61, 549 – 555, <https://doi.org/10.1007/s10872-005-0062-y>, 2005b.
- Dee, D. P., Uppala, S. M., Simmons, A. J., Berrisford, P., Poli, P., Kobayashi, S., Andrae, U., Balmaseda, M. A., Balsamo, G., Bauer, P., Bechtold, P., Beljaars, A. C., van de Berg, L., Bidlot, J., Bormann, N., Delsol, C., Dragani, R., Fuentes, M., Geer, A. J., Haim-

- berger, L., Healy, S. B., Hersbach, H., Hólm, E. V., Isaksen, I., Kållberg, P., Köhler, M., Matricardi, M., McNally, A. P., Monge-Sanz, B. M., Morcrette, J. J., Park, B. K., Peubey, C., de Rosnay, P., Tavolato, C., Thépaut, J. N., and Vitart, F.: The ERA-Interim reanalysis: Configuration and performance of the data assimilation system, *Quarterly Journal of the Royal Meteorological Society*, 137, 553–597, <https://doi.org/10.1002/qj.828>, 2011.
- Desbruyères, D., Thierry, V., and Mercier, H.: Simulated decadal variability of the meridional overturning circulation across the A25-Ovide section, *Journal of Geophysical Research: Oceans*, 118, 462–475, <https://doi.org/10.1029/2012JC008342>, 2013.
- Desbruyères, D., Mercier, H., and Thierry, V.: On the mechanisms behind decadal heat content changes in the eastern subpolar gyre, *Progress in Oceanography*, 132, 262–272, <https://doi.org/10.1016/j.pocean.2014.02.005>, 2015.
- Desbruyères, D., Chafik, L., and Maze, G.: A shift in the ocean circulation has warmed the subpolar North Atlantic Ocean since 2016, *Communications Earth & Environment*, 2, <https://doi.org/10.1038/s43247-021-00120-y>, 2021.
- Desbruyères, D. G., Mercier, H., Maze, G., and Danialt, N.: Surface predictor of overturning circulation and heat content change in the subpolar North Atlantic, *Ocean Science*, 15, 809–817, <https://doi.org/10.5194/os-15-809-2019>, 2019.
- Dickson, R. R. and Brown, J.: The production of North Atlantic Deep Water: sources, rates, and pathways, *Journal of Geophysical Research*, 99, <https://doi.org/10.1029/94jc00530>, 1994.
- Döös, K., Kjellsson, J., and Jönsson, B.: TRACMASS—A Lagrangian Trajectory Model, pp. 225–249, Springer International Publishing, Heidelberg, [https://doi.org/10.1007/978-3-319-00440-2\\_7](https://doi.org/10.1007/978-3-319-00440-2_7), 2013.
- Döös, K., Jönsson, B., and Kjellsson, J.: Evaluation of oceanic and atmospheric trajectory schemes in the TRACMASS trajectory model v6.0, *Geoscientific Model Development*, 10, 1733–1749, <https://doi.org/10.5194/gmd-10-1733-2017>, 2017.
- Eldevik, T., Nilsen, J. E., Iovino, D., Anders Olsson, K., Sandø, A. B., and Drange, H.: Observed sources and variability of Nordic seas overflow, *Nature Geoscience*, 2, 406–410, <https://doi.org/10.1038/ngeo518>, 2009.
- Evans, D. G., Toole, J., Forget, G., Zika, J. D., Garabato, A. C. N., Nurser, A. J. G., and Yu, L.: Recent Wind-Driven Variability in Atlantic Water Mass Distribution and Meridional Overturning Circulation, *Journal of Physical Oceanography*, 47, 633 – 647, <https://doi.org/10.1175/JPO-D-16-0089.1>, 2017.
- Evans, D. G., Holliday, N. P., Bacon, S., and Bras, I. L.: Mixing and air-sea buoyancy fluxes set the time-mean overturning circulation in the subpolar North Atlantic, *Ocean Sciences*, EGU sphere [preprint], <https://doi.org/10.5194/egusphere-2022-1059>, 2022.
- Fay, A. R. and McKinley, G. A.: Observed Regional Fluxes to Constrain Modeled Estimates of the Ocean Carbon Sink, *Geophysical Research Letters*, 48, e2021GL095325, <https://doi.org/https://doi.org/10.1029/2021GL095325>, 2021.
- Fichefet, T. and Morales Maqueda, M. A.: Modelling the influence of snow accumulation and snow-ice formation on the seasonal cycle of the Antarctic sea-ice cover, *Climate Dynamics*, 15, 251–268, <https://doi.org/10.1007/s003820050280>, 1999.
- Flatau, M. K., Talley, L., and Niiler, P. P.: The North Atlantic Oscillation, surface current velocities, and SST changes in the subpolar North Atlantic, *Journal of Climate*, 16, 2355–2369, <https://doi.org/10.1175/2787.1>, 2003.
- Fofonoff, N. P. and Millard, R. C.: Algorithms for computation of fundamental properties of seawater, UNESCO Technical papers in marine science, 44, 53, <http://darchive.mblwhoilibrary.org:8080/handle/1912/2470>, 1983.
- Foukal, N. P., Gelderloos, R., and Pickart, R. S.: A continuous pathway for fresh water along the East Greenland shelf, *Science Advances*, 6, eabc4254, <https://doi.org/10.1126/sciadv.abc4254>, 2020.
- Frajka-Williams, E., Ansorge, I. J., Baehr, J., Bryden, H. L., Chidichimo, M. P., Cunningham, S. A., Danabasoglu, G., Dong, S., Donohue, K. A., Elipot, S., Heimbach, P., Holliday, N. P., Hummels, R., Jackson, L. C., Karstensen, J., Lankhorst, M., Le Bras, I. A., Susan Lozier, M., McDonagh, E. L., Meinen, C. S., Mercier, H., Moat, B. I., Perez, R. C., Piecuch, C. G., Rhein, M., Srokosz, M. A., Trenberth, K. E.,

- Bacon, S., Forget, G., Goni, G., Kieke, D., Koelling, J., Lamont, T., McCarthy, G. D., Mertens, C., Send, U., Smeed, D. A., Speich, S., van den Berg, M., Volkov, D., and Wilson, C.: Atlantic meridional overturning circulation: Observed transport and variability, *Frontiers in Marine Science*, 6, 1–18, <https://doi.org/10.3389/fmars.2019.00260>, 2019.
- 1145 Fried, N. and de Jong, M. F.: The Role of the Irminger Current in the Irminger Sea Northward Transport Variability, *Journal of Geophysical Research: Oceans*, 127, 1–16, <https://doi.org/10.1029/2021JC018188>, 2022.
- Fu, Y., Feili, L., Karstensen, J., and Wang, C.: A stable Atlantic Meridional Overturning Circulation in a changing North Atlantic Ocean since the 1990s, *Science Advances*, 6, <https://doi.org/10.1126/sciadv.abc7836>, 2020.
- 1150 Gary, S. F., Susan Lozier, M., Böning, C. W., and Biastoch, A.: Deciphering the pathways for the deep limb of the Meridional Overturning Circulation, *Deep Sea Research Part II: Topical Studies in Oceanography*, 58, 1781–1797, <https://doi.org/https://doi.org/10.1016/j.dsr2.2010.10.059>, 2011.
- Gent, P. R. and McWilliams, J. C.: Isopycnal Mixing in Ocean Circulation Models, *Journal of Physical Oceanography*, 20, 150 – 155, [https://doi.org/10.1175/1520-0485\(1990\)020<0150:IMIOCM>2.0.CO;2](https://doi.org/10.1175/1520-0485(1990)020<0150:IMIOCM>2.0.CO;2), 1990.
- 1155 Georgiou, S., Ypma, S. L., Brüggemann, N., Sayol, J., van der Boog, C. G., Spence, P., Pietrzak, J. D., and Katsman, C. A.: Direct and Indirect Pathways of Convected Water Masses and Their impacts on the Overturning Dynamics of the Labrador Sea, *Journal of Geophysical Research: Oceans*, 126, 1–19, <https://doi.org/10.1029/2020jc016654>, 2021.
- Grist, J. P., Josey, S. A., Jacobs, Z. L., Marsh, R., Sinha, B., and Van Sebille, E.: Extreme air–sea interaction over the North Atlantic subpolar gyre during the winter of 2013–2014 and its sub-surface legacy, *Climate Dynamics*, 46, 4027–4045, [https://doi.org/10.1007/s00382-015-](https://doi.org/10.1007/s00382-015-2819-3)
- 1160 2819-3, 2016.
- Groeskamp, S., Zika, J. D., Sloyan, B. M., McDougall, T. J., and McIntosh, P. C.: A Thermohaline Inverse Method for Estimating Diathermohaline Circulation and Mixing, *Journal of Physical Oceanography*, 44, 2681 – 2697, <https://doi.org/10.1175/JPO-D-14-0039.1>, 2014.
- Heuzé, C.: North Atlantic deep water formation and AMOC in CMIP5 models, *Ocean Science*, 13, 609–622, [https://doi.org/10.5194/os-13-](https://doi.org/10.5194/os-13-609-2017)
- 609-2017, 2017.
- 1165 Heuzé, C.: Antarctic Bottom Water and North Atlantic Deep Water in CMIP6 models, *Ocean Science*, 17, 59–90, [https://doi.org/10.5194/os-](https://doi.org/10.5194/os-17-59-2021)
- 17-59-2021, 2021.
- Hirschi, J. J.-M., Barnier, B., Böning, C., Biastoch, A., Blaker, A. T., Coward, A., Danilov, S., Drijfhout, S., Getzlaff, K., Griffies, S. M., Hasumi, H., Hewitt, H., Iovino, D., Kawasaki, T., Kiss, A. E., Koldunov, N., Marzocchi, A., Mecking, J. V., Moat, B., Molines, J.-M., Myers, P. G., Penduff, T., Roberts, M., Treguier, A.-M., Sein, D. V., Sidorenko, D., Small, J., Spence, P., Thompson, L., Weijer, W., and
- 1170 Xu, X.: The Atlantic Meridional Overturning Circulation in High-Resolution Models, *Journal of Geophysical Research: Oceans*, 125, e2019JC015 522, <https://doi.org/https://doi.org/10.1029/2019JC015522>, 2020.
- Holliday, N. P., Hughes, S. L., Bacon, S., Beszczynska-Möller, A., Hansen, B., Lavín, A., Loeng, H., Mork, K. A., Østerhus, S., Sherwin, T., and Walczowski, W.: Reversal of the 1960s to 1990s freshening trend in the northeast North Atlantic and Nordic Seas, *Geophysical Research Letters*, 35, 1–5, <https://doi.org/10.1029/2007GL032675>, 2008.
- 1175 Holliday, N. P., Bacon, S., Cunningham, S. A., Gary, S. F., Karstensen, J., King, B. A., Li, F., and Mcdonagh, E. L.: Subpolar North Atlantic Overturning and Gyre-Scale Circulation in the Summers of 2014 and 2016, *Journal of Geophysical Research: Oceans*, 123, 4538–4559, <https://doi.org/10.1029/2018JC013841>, 2018.
- Holliday, N. P., Bersch, M., Berx, B., Chafik, L., Cunningham, S., Florindo-López, C., Hátún, H., Johns, W., Josey, S. A., Larsen, K. M. H., Mulet, S., Oltmanns, M., Reverdin, G., Rossby, T., Thierry, V., Valdimarsson, H., and Yashayaev, I.: Ocean circulation causes the

- 1180 largest freshening event for 120 years in eastern subpolar North Atlantic, *Nature Communications*, 11, <https://doi.org/10.1038/s41467-020-14474-y>, 2020.
- Holte, J. and Straneo, F.: Seasonal overturning of the Labrador sea as observed by Argo floats, *Journal of Physical Oceanography*, 47, 2531–2543, <https://doi.org/10.1175/JPO-D-17-0051.1>, 2017.
- Houpert, L., Inall, M. E., Dumont, E., Gary, S., Johnson, C., Porter, M., Johns, W. E., and Cunningham, S. A.: Structure and Transport of  
1185 the North Atlantic Current in the Eastern Subpolar Gyre From Sustained Glider Observations, *Journal of Geophysical Research: Oceans*, 123, 6019–6038, <https://doi.org/10.1029/2018JC014162>, 2018.
- Houpert, L., Cunningham, S., Fraser, N., Johnson, C., Holliday, N. P., Jones, S., Moat, B., and Rayner, D.: Observed Variability of the North Atlantic Current in the Rockall Trough From 4 Years of Mooring Measurements, *Journal of Geophysical Research: Oceans*, 125, e2020JC016403, <https://doi.org/https://doi.org/10.1029/2020JC016403>, 2020.
- 1190 Huang, J., Pickart, R. S., Bahr, F., McRaven, L. T., and Xu, F.: Wintertime Water Mass Transformation in the Western Iceland and Greenland Seas, *Journal of Geophysical Research: Oceans*, 126, 1–19, <https://doi.org/10.1029/2020JC016893>, 2021.
- Hurrell, J.: Decadal Trends in the North Atlantic Oscillation: Regional Temperatures and Precipitation, *Science*, 269, 676–679, <https://doi.org/10.1126/science.269.5224.676>, 1995.
- Isachsen, P. E., Mauritzen, C., and Svendsen, H.: Dense water formation in the Nordic Seas diagnosed from sea surface buoyancy fluxes,  
1195 Deep-Sea Research Part I: Oceanographic Research Papers, 54, 22–41, <https://doi.org/10.1016/j.dsr.2006.09.008>, 2007.
- Jackson, L. C., Roberts, M. J., Hewitt, H. T., Iovino, D., Koenig, T., Meccia, V. L., Roberts, C. D., Ruprich-Robert, Y., and Wood, R. A.: Impact of ocean resolution and mean state on the rate of AMOC weakening, *Climate Dynamics*, 55, 1711–1732, <https://doi.org/10.1007/s00382-020-05345-9>, 2020.
- Kieke, D., Rhein, M., Stramma, L., Smethie, W. M., Bullister, J. L., and LeBel, D. A.: Changes in the pool of Labrador Sea Water in the  
1200 subpolar North Atlantic, *Geophysical Research Letters*, 34, 1–5, <https://doi.org/10.1029/2006GL028959>, 2007.
- Lavender, K. L., Davis, R. E., and Owens, W. B.: Mid-depth recirculation observed in the interior Labrador and Irminger seas by direct velocity measurements, *Nature*, 407, 66–69, <https://doi.org/10.1038/35024048>, 2000.
- Le Bras, I. A., Straneo, F., Holte, J., de Jong, M. F., and Holliday, N. P.: Rapid Export of Waters Formed by Convection Near the Irminger Sea’s Western Boundary, *Geophysical Research Letters*, 47, <https://doi.org/10.1029/2019GL085989>, 2020.
- 1205 Le Bras, I. A.-A., Straneo, F., Holte, J., and Holliday, N. P.: Seasonality of Freshwater in the East Greenland Current System From 2014 to 2016, *Journal of Geophysical Research: Oceans*, 123, 8828–8848, <https://doi.org/https://doi.org/10.1029/2018JC014511>, 2018.
- Levitus, S., Boyer, T., Conkright, M., O’Brien, T., Antonov, J., Stephens, C., Stathoplos, L., Johnson, D., and Gelfeld, R.: World Ocean Database 1998, Tech. rep., 1998.
- Lherminier, P., Mercier, H., Gourcuff, C., Alvarez, M., Bacon, S., and Kermabon, C.: Transports across the 2002 Greenland-Portugal Ovide  
1210 section and comparison with 1997, *Journal of Geophysical Research: Oceans*, 112, 1–20, <https://doi.org/10.1029/2006JC003716>, 2007.
- Li, F., Lozier, M. S., and Johns, W. E.: Calculating the meridional volume, heat, and freshwater transports from an observing system in the subpolar North Atlantic: Observing system simulation experiment, *Journal of Atmospheric and Oceanic Technology*, 34, 1483–1500, <https://doi.org/10.1175/JTECH-D-16-0247.1>, 2017.
- Li, F., Lozier, M., Danabasoglu, G., Holliday, P., Kwon, O., Romanou, A., Yeager, S. G., and Zhang, R.: Local and downstream relationships  
1215 between labrador sea water volume and North Atlantic meridional overturning circulation variability, *Journal of Climate*, 32, 3883–3898, <https://doi.org/10.1175/JCLI-D-18-0735.1>, 2019.

- Li, F., Lozier, M. S., Bacon, S., Bower, A. S., Cunningham, S. A., de Jong, M. F., DeYoung, B., Fraser, N., Fried, N., Han, G., Holliday, N. P., Holte, J., Houpert, L., Inall, M. E., Johns, W. E., Jones, S., Johnson, C., Karstensen, J., Le Bras, I. A., Lherminier, P., Lin, X., Mercier, H., Oltmanns, M., Pacini, A., Petit, T., Pickart, R. S., Rayner, D., Straneo, F., Thierry, V., Visbeck, M., Yashayaev, I., and Zhou, C.: Subpolar North Atlantic western boundary density anomalies and the Meridional Overturning Circulation, *Nature Communications*, 12, 1–9, <https://doi.org/10.1038/s41467-021-23350-2>, 2021a.
- Li, F., Lozier, M. S., Holliday, N. P., Johns, W. E., Le Bras, I. A., Moat, B. I., Cunningham, S. A., and de Jong, M. F.: Observation-based estimates of heat and freshwater exchanges from the subtropical North Atlantic to the Arctic, *Progress in Oceanography*, 197, 102640, <https://doi.org/https://doi.org/10.1016/j.pocean.2021.102640>, 2021b.
- 1225 Lin, P., Pickart, R. S., Torres, D. J., and Pacini, A.: Evolution of the freshwater coastal current at the Southern Tip of Greenland, *Journal of Physical Oceanography*, 48, 2127–2140, <https://doi.org/10.1175/JPO-D-18-0035.1>, 2018.
- Lozier, M., Leadbetter, S., Williams, R., Roussenov, V., Reed, M., and Moore, N.: The Spatial Pattern and Mechanisms of Heat-Content Change in the North Atlantic, *Science*, 319, 800–803, <https://doi.org/10.1126/science.1146436>, 2008.
- Lozier, M. S., Bacon, S., Bower, A. S., Cunningham, S. A., De Jong, M. F., De Steur, L., De Young, B., Fischer, J., Gary, S. F., Greenan, B. J., Heimbmbach, P., Holliday, N. P., Houpert, L., Inall, M. E., Johns, W. E., Johnson, H. L., Karstensen, J., Li, F., Lin, X., Mackay, N., Marshall, D. P., Mercier, H., Myers, P. G., Pickart, R. S., Pillar, H. R., Straneo, F., Thierry, V., Weller, R. A., Williams, R. G., Wilson, C., Yang, J., Zhao, J., and Zika, J. D.: Overturning in the Subpolar north Atlantic program: A new international ocean observing system, *Bulletin of the American Meteorological Society*, 98, 737–752, <https://doi.org/10.1175/BAMS-D-16-0057.1>, 2017.
- 1230 Lozier, M. S., Li, F., Bacon, S., Bahr, F., Bower, A. S., Cunningham, S. A., De Jong, M. F., De Steur, L., DeYoung, B., Fischer, J., Gary, S. F., Greenan, B. J., Holliday, N. P., Houk, A., Houpert, L., Inall, M. E., Johns, W. E., Johnson, H. L., Johnson, C., Karstensen, J., Koman, G., Le Bras, I. A., Lin, X., Mackay, N., Marshall, D. P., Mercier, H., Oltmanns, M., Pickart, R. S., Ramsey, A. L., Rayner, D., Straneo, F., Thierry, V., Torres, D. J., Williams, R. G., Wilson, C., Yang, J., Yashayaev, I., and Zhao, J.: A sea change in our view of overturning in the subpolar North Atlantic, *Science*, 363, 516–521, <https://doi.org/10.1126/science.aau6592>, 2019.
- 1235 MacGilchrist, G. A., Johnson, H. L., Marshall, D. P., Lique, C., Thomas, M., Jackson, L. C., and Wood, R. A.: Locations and mechanisms of ocean ventilation in the high-latitude north atlantic in an eddy-permitting ocean model, *Journal of Climate*, 33, 10113–10131, <https://doi.org/10.1175/JCLI-D-20-0191.1>, 2020.
- MacGilchrist, G. A., Johnson, H. L., Lique, C., and Marshall, D. P.: Demons in the North Atlantic: Variability of Deep Ocean Ventilation, *Geophysical Research Letters*, 48, 1–9, <https://doi.org/10.1029/2020GL092340>, 2021.
- Mackay, N., Wilson, C., Holliday, N. P., and Zika, J. D.: The Observation-Based Application of a Regional Thermohaline Inverse Method to Diagnose the Formation and Transformation of Water Masses North of the OSNAP Array from 2013 to 2015, *Journal of Physical Oceanography*, 50, 1533 – 1555, <https://doi.org/10.1175/JPO-D-19-0188.1>, 2020.
- 1245 Madec, G.: NEMO Ocean Engine. Note du Pôle Modélisation de l’Institut Pierre-Simon Laplace 27, Tech. rep., 2014.
- Marzocchi, A., Hirschi, J. J.-M., Holliday, N. P., Cunningham, S. A., Blaker, A. T., and Coward, A. C.: The North Atlantic subpolar circulation in an eddy-resolving global ocean model, *Journal of Marine Systems*, 142, 126–143, <https://doi.org/https://doi.org/10.1016/j.jmarsys.2014.10.007>, 2015.
- 1250 Mauritzen, C.: Production of dense overflow waters feeding the North Atlantic across the Greenland-Scotland Ridge. Part 1: Evidence for a revised circulation scheme, *Deep-Sea Research Part I: Oceanographic Research Papers*, 43, 769–806, [https://doi.org/10.1016/0967-0637\(96\)00037-4](https://doi.org/10.1016/0967-0637(96)00037-4), 1996.

- 1255 McCartney, M. S. and Talley, L. D.: The Subpolar Mode Water of the North Atlantic Ocean, *Journal of Physical Oceanography*, 12, 1169–1188, 1982.
- McKinley, G. A., Fay, A. R., Lovenduski, N. S., and Pilcher, D. J.: Natural Variability and Anthropogenic Trends in the Ocean Carbon Sink, *Annual Review of Marine Science*, 9, 125–150, <https://doi.org/10.1146/annurev-marine-010816-060529>, 2017.
- Medhaug, I., Langehaug, H. R., Eldevik, T., Furevik, T., and Bentsen, M.: Mechanisms for decadal scale variability in a simulated Atlantic meridional overturning circulation, *Climate Dynamics*, 39, 77–93, <https://doi.org/10.1007/s00382-011-1124-z>, 2012.
- 1260 Menary, M. B., Hodson, D. L., Robson, J. I., Sutton, R. T., Wood, R. A., and Hunt, J. A.: Exploring the impact of CMIP5 model biases on the simulation of North Atlantic decadal variability, *Geophysical Research Letters*, 42, 5926–5934, <https://doi.org/10.1002/2015GL064360>, 2015.
- Menary, M. B., Jackson, L. C., and Lozier, M. S.: Reconciling the Relationship Between the AMOC and Labrador Sea in OSNAP Observations and Climate Models, *Geophysical Research Letters*, 47, <https://doi.org/10.1029/2020GL089793>, 2020.
- 1265 Mercier, H., Lherminier, P., Sarafanov, A., Gaillard, F., Daniault, N., Desbruyères, D., Falina, A., Ferron, B., Gourcuff, C., Huck, T., and Thierry, V.: Variability of the meridional overturning circulation at the Greenland-Portugal OVIDE section from 1993 to 2010, *Progress in Oceanography*, 132, 250–261, <https://doi.org/10.1016/j.pocean.2013.11.001>, 2015.
- Mielke, C., Frajka-Williams, E., and Baehr, J.: Observed and simulated variability of the AMOC at 26°N and 41°N, *Geophysical Research Letters*, 40, 1159–1164, <https://doi.org/10.1002/grl.50233>, 2013.
- 1270 Molines, J.-M.: meom-configurations/ORCA025.L75-GJM189 (V-1.1). Zenodo., <https://doi.org/10.5281/zenodo.4626012>, 2021.
- Østerhus, S., Woodgate, R., Valdimarsson, H., Turrell, B., De Steur, L., Quadfasel, D., Olsen, S. M., Moritz, M., Lee, C. M., Larsen, K. M. H., Jónsson, S., Johnson, C., Jochumsen, K., Hansen, B., Curry, B., Cunningham, S., and Berx, B.: Arctic Mediterranean exchanges: A consistent volume budget and trends in transports from two decades of observations, *Ocean Science*, 15, 379–399, <https://doi.org/10.5194/os-15-379-2019>, 2019.
- 1275 Pacini, A., Pickart, R. S., Bahr, F., Torres, D. J., Ramsey, A. L., Holte, J., Karstensen, J., Oltmanns, M., Straneo, F., Bras, I. A. L., Moore, G. W. K., and de Jong, M. F.: Mean Conditions and Seasonality of the West Greenland Boundary Current System near Cape Farewell, *Journal of Physical Oceanography*, 50, 2849 – 2871, <https://doi.org/10.1175/JPO-D-20-0086.1>, 2020.
- Paris, C. B., Helgers, J., van Sebille, E., and Srinivasan, A.: Connectivity Modeling System: A probabilistic modeling tool for the multi-scale tracking of biotic and abiotic variability in the ocean, *Environmental Modelling & Software*, 42, 47–54, <https://doi.org/https://doi.org/10.1016/j.envsoft.2012.12.006>, 2013.
- 1280 Pennelly, C. and Myers, P. G.: Introducing LAB60: A 1/60° NEMO 3.6 numerical simulation of the Labrador Sea, *Geoscientific Model Development*, 13, 4959–4975, <https://doi.org/10.5194/gmd-13-4959-2020>, 2020.
- Petit, T., Lozier, M. S., Josey, S. A., and Cunningham, S. A.: Atlantic Deep Water Formation Occurs Primarily in the Iceland Basin and Irminger Sea by Local Buoyancy Forcing, *Geophysical Research Letters*, 47, <https://doi.org/10.1029/2020GL091028>, 2020.
- 1285 Pickart, R. S. and Spall, M. A.: Impact of Labrador Sea convection on the North Atlantic meridional overturning circulation, *Journal of Physical Oceanography*, 37, 2207–2227, <https://doi.org/10.1175/JPO3178.1>, 2007.
- Pickart, R. S., Spall, M. A., and Lazier, J. R.: Mid-depth ventilation in the western boundary current system of the sub-polar gyre, *Deep-Sea Research Part I: Oceanographic Research Papers*, 44, 1025–1054, [https://doi.org/10.1016/S0967-0637\(96\)00122-7](https://doi.org/10.1016/S0967-0637(96)00122-7), 1997.
- Piron, A., Thierry, V., Mercier, H., and Caniaux, G.: Argo float observations of basin-scale deep convection in the Irminger sea during winter 2011–2012, *Deep-Sea Research Part I: Oceanographic Research Papers*, 109, 76–90, <https://doi.org/10.1016/j.dsr.2015.12.012>, 2016.
- 1290

- Pollard, R. T., Read, J. F., Holliday, N. P., and Leach, H.: Water masses and circulation pathways through the Iceland Basin during Vivaldi 1996, *Journal of Geophysical Research: Oceans*, 109, <https://doi.org/https://doi.org/10.1029/2003JC002067>, 2004.
- Read, J. F.: CONVEX-91: Water masses and circulation of the Northeast Atlantic subpolar gyre, *Progress in Oceanography*, 48, 461–510, [https://doi.org/10.1016/S0079-6611\(01\)00011-8](https://doi.org/10.1016/S0079-6611(01)00011-8), 2000.
- 1295 Rhein, M., Kieke, D., and Steinfeldt, R.: Advection of North Atlantic Deep Water from the Labrador Sea to the southern hemisphere, *Journal of Geophysical Research: Oceans*, 120, 2471–2487, <https://doi.org/10.1002/2014JC010605>, 2015.
- Sarafanov, A., Mercier, H., Falina, A., Sokov, A., and Lherminier, P.: Cessation and partial reversal of deep water freshening in the northern North Atlantic: Observation-based estimates and attribution, *Tellus, Series A: Dynamic Meteorology and Oceanography*, 62, 80–90, <https://doi.org/10.1111/j.1600-0870.2009.00418.x>, 2010.
- 1300 Sarafanov, A., Falina, A., Mercier, H., Sokov, A., Lherminier, P., Gourcuff, C., Gladyshev, S., Gaillard, F., and Daniault, N.: Mean full-depth summer circulation and transports at the northern periphery of the Atlantic Ocean in the 2000s, *Journal of Geophysical Research: Oceans*, 117, 1–22, <https://doi.org/10.1029/2011JC007572>, 2012.
- Spall, M. A.: Boundary currents and watermass transformation in marginal seas, *Journal of Physical Oceanography*, 34, 1197–1213, [https://doi.org/10.1175/1520-0485\(2004\)034<1197:BCAWTI>2.0.CO;2](https://doi.org/10.1175/1520-0485(2004)034<1197:BCAWTI>2.0.CO;2), 2004.
- 1305 Steele, M., Morley, R., and Ermold, W.: PHC: a global hydrography with a high quality Arctic Ocean., *Journal of Climate*, 14, 2079–2087, <https://www.jstor.org/stable/26247422>, 2001.
- Stommel, H.: Determination of water mass properties of water pumped down from the Ekman layer to the geostrophic flow below, *Proceedings of the National Academy of Sciences*, 76, 3051–3055, <https://doi.org/10.1073/pnas.76.7.3051>, 1979.
- Sutherland, D. A. and Pickart, R. S.: The East Greenland Coastal Current: Structure, variability, and forcing, *Progress in Oceanography*, 78, 58–77, <https://doi.org/10.1016/j.pocean.2007.09.006>, 2008.
- 1310 Sutherland, D. A., Pickart, R. S., Peter Jones, E., Azetsu-Scott, K., Jane Eert, A., and Ólafsson, J.: Freshwater composition of the waters off southeast Greenland and their link to the Arctic Ocean, *Journal of Geophysical Research: Oceans*, 114, <https://doi.org/https://doi.org/10.1029/2008JC004808>, 2009.
- Tamsitt, V., Abernathey, R. P., Mazloff, M. R., Wang, J., and Talley, L. D.: Transformation of Deep Water Masses Along Lagrangian Upwelling Pathways in the Southern Ocean, *Journal of Geophysical Research: Oceans*, 123, 1994–2017, <https://doi.org/10.1002/2017JC013409>, 2018.
- 1315 Thierry, V., de Boisséon, E., and Mercier, H.: Interannual variability of the Subpolar Mode Water properties over the Reykjanes Ridge during 1990-2006, *Journal of Geophysical Research: Oceans*, 113, 1–14, <https://doi.org/10.1029/2007JC004443>, 2008.
- Tooth, O. J., Johnson, H. L., and Wilson, C.: Lagrangian Overturning Pathways in the Eastern Subpolar North Atlantic, *Journal of Climate*, 36, 823 – 844, <https://doi.org/10.1175/JCLI-D-21-0985.1>, 2023.
- 1320 Treguier, A. M., Theetten, S., Chassignet, E. P., Penduff, T., Smith, R., Talley, L., Beismann, J. O., and Böning, C.: The North Atlantic Subpolar Gyre in Four High-Resolution Models, *Journal of Physical Oceanography*, 35, 757 – 774, <https://doi.org/10.1175/JPO2720.1>, 2005.
- Uppala, S. M., Kållberg, P. W., Simmons, A. J., Andrae, U., da Costa Bechtold, V., Fiorino, M., Gibson, J. K., Haseler, J., Hernandez, A., 1325 Kelly, G. A., Li, X., Onogi, K., Saarinen, S., Sokka, N., Allan, R. P., Andersson, E., Arpe, K., Balmaseda, M. A., Beljaars, A. C., van de Berg, L., Bidlot, J., Bormann, N., Caires, S., Chevallier, F., Dethof, A., Dragosavac, M., Fisher, M., Fuentes, M., Hagemann, S., Hólm, E., Hoskins, B. J., Isaksen, L., Janssen, P. A., Jenne, R., McNally, A. P., Mahfouf, J. F., Morcrette, J. J., Rayner, N. A., Saunders, R. W.,



- Simon, P., Sterl, A., Trenberth, K. E., Untch, A., Vasiljevic, D., Viterbo, P., and Woollen, J.: The ERA-40 re-analysis, *Quarterly Journal of the Royal Meteorological Society*, 131, 2961–3012, <https://doi.org/10.1256/qj.04.176>, 2005.
- 1330 Våge, K., Pickart, R. S., Moore, G. W., and Ribergaard, M. H.: Winter mixed layer development in the central Irminger Sea: The effect of strong, intermittent wind events, *Journal of Physical Oceanography*, 38, 541–565, <https://doi.org/10.1175/2007JPO3678.1>, 2008.
- Våge, K., Pickart, R. S., Sarafanov, A., Knutsen, Ø., Mercier, H., Lherminier, P., van Aken, H. M., Meincke, J., Quadfasel, D., and Bacon, S.: The Irminger Gyre: Circulation, convection, and interannual variability, *Deep-Sea Research Part I: Oceanographic Research Papers*, 58, 590–614, <https://doi.org/10.1016/j.dsr.2011.03.001>, 2011.
- 1335 Våge, K., Moore, G. W., Jónsson, S., and Valdimarsson, H.: Water mass transformation in the iceland sea, *Deep-Sea Research Part I: Oceanographic Research Papers*, 101, 98–109, <https://doi.org/10.1016/j.dsr.2015.04.001>, 2015.
- Van Aken, H. M. and De Boer, C. J.: On the synoptic hydrography of intermediate and deep water masses in the Iceland Basin, *Deep-Sea Research Part I*, 42, 165–189, [https://doi.org/10.1016/0967-0637\(94\)00042-Q](https://doi.org/10.1016/0967-0637(94)00042-Q), 1995.
- Visbeck, M., Chassignet, E. P., Curry, R. G., Delworth, T. L., Dickson, R. R., and Krahnmann, G.: The Ocean's Response to North Atlantic Oscillation Variability, pp. 113–145, *American Geophysical Union (AGU)*, <https://doi.org/https://doi.org/10.1029/134GM06>, 2003.
- 1340 Wåhlin, A. K. and Johnson, H. L.: The salinity, heat, and buoyancy budgets of a coastal current in a marginal sea, *Journal of Physical Oceanography*, 39, 2562–2580, <https://doi.org/10.1175/2009JPO4090.1>, 2009.
- Wang, H., Zhao, J., Li, F., and Lin, X.: Seasonal and Interannual Variability of the Meridional Overturning Circulation in the Subpolar North Atlantic Diagnosed From a High Resolution Reanalysis Data Set, *Journal of Geophysical Research: Oceans*, 126, e2020JC017 130, <https://doi.org/https://doi.org/10.1029/2020JC017130>, 2021.
- 1345 Williams, R., Marshall, J., and M.A., S.: Does Stommel's Mixed Layer "Demon" Work?, *Journal of Physical Oceanography*, 25, 3089–3102, [https://doi.org/10.1175/1520-0485\(1995\)025<3089:dsmlw>2.0.co;2](https://doi.org/10.1175/1520-0485(1995)025<3089:dsmlw>2.0.co;2), 1995.
- Willis, J. K.: Can in situ floats and satellite altimeters detect long-term changes in Atlantic Ocean overturning?, *Geophysical Research Letters*, <https://doi.org/10.1029/2010GL042372>, 2010.
- 1350 Xu, X., Hurlburt, H. E., Schmitz, W. J., Zantopp, R., Fischer, J., and Hogan, P. J.: On the currents and transports connected with the atlantic meridional overturning circulation in the subpolar North Atlantic, *Journal of Geophysical Research: Oceans*, 118, 502–516, <https://doi.org/10.1002/jgrc.20065>, 2013.
- Xu, X., Chassignet, E., Johns, W., Schmitz Jr, W., and Metzger, J.: Intraseasonal to interannual variability of the Atlantic meridional overturning circulation from eddy-resolving simulations and observations, *Journal of Geophysical Research: Oceans*, pp. 5140–5159, <https://doi.org/10.1002/2014JC009994>, 2014.
- 1355 Xu, X., Bower, A., Furey, H., and Chassignet, E. P.: Variability of the Iceland-Scotland Overflow Water Transport Through the Charlie-Gibbs Fracture Zone: Results From an Eddy Simulation and Observations, *Journal of Geophysical Research: Oceans*, 123, 5808–5823, <https://doi.org/10.1029/2018JC013895>, 2018a.
- Xu, X., Rhines, P. B., and Chassignet, E. P.: On mapping the diapycnal water mass transformation of the upper North Atlantic Ocean, *Journal of Physical Oceanography*, 48, 2233–2258, <https://doi.org/10.1175/JPO-D-17-0223.1>, 2018b.
- 1360 Zhang, R. and Thomas, M.: Horizontal circulation across density surfaces contributes substantially to the long-term mean northern Atlantic Meridional Overturning Circulation, *Communications Earth & Environment*, 2, <https://doi.org/10.1038/s43247-021-00182-y>, 2021.